

Engineered extrachromosomal oncogene amplifications promote tumorigenesis

<https://doi.org/10.1038/s41586-024-08318-8>

Received: 22 June 2023

Accepted: 31 October 2024

Published online: 18 December 2024

Open access

 Check for updates

Davide Pradella^{1,16}, Minsi Zhang^{1,2,16}, Rui Gao^{1,3,16}, Melissa A. Yao^{1,3,16}, Katarzyna M. Gluchowska¹, Ylenia Cendon-Florez¹, Tanmay Mishra^{1,4}, Gaspare La Rocca¹, Moritz Weigl¹, Ziqi Jiao^{1,3}, Hieu H. M. Nguyen¹, Marta Lisi⁵, Mateusz M. Ozimek¹, Chiara Mastrolorenzo¹, Kevin Chen¹, Felix Grimm¹, Jens Luebeck⁶, Shu Zhang^{7,8,9,10}, Andrea Alice Zolli¹, Eric G. Sun¹¹, Bhargavi Dameracharla⁶, Zhengqiao Zhao¹², Yuri Pritykin¹², Carlie Sigel¹³, Howard Y. Chang^{7,8,14}, Paul S. Mischel^{9,10}, Vineet Bafna^{6,15}, Cristina R. Antonescu¹³ & Andrea Ventura¹✉

Focal gene amplifications are among the most common cancer-associated mutations¹ but have proven challenging to engineer in primary cells and model organisms. Here we describe a general strategy to engineer large (more than 1 Mbp) focal amplifications mediated by extrachromosomal DNAs (ecDNAs)² in a spatiotemporally controlled manner in cells and in mice. By coupling ecDNA formation with expression of selectable markers, we track the dynamics of ecDNA-containing cells under physiological conditions and in the presence of specific selective pressures. We also apply this approach to generate mice harbouring Cre-inducible *Myc*- and *Mdm2*-containing ecDNAs analogous to those occurring in human cancers. We show that the engineered ecDNAs spontaneously accumulate in primary cells derived from these animals, promoting their proliferation, immortalization and transformation. Finally, we demonstrate the ability of *Mdm2*-containing ecDNAs to promote tumour formation in an autochthonous mouse model of hepatocellular carcinoma. These findings offer insights into the role of ecDNA-mediated gene amplifications in tumorigenesis. We anticipate that this approach will be valuable for investigating further unresolved aspects of ecDNA biology and for developing new preclinical immunocompetent mouse models of human cancers harbouring specific focal gene amplifications.

Engineering cancer-associated genetic lesions in cells and in model organisms is essential to defining their contribution to tumour initiation and progression and to the development of accurate preclinical models of human cancers. Over the past few decades, advances in germline and somatic gene editing methods have substantially improved our ability to model a wide range of loss- and gain-of-function mutations in a temporally and spatially controlled fashion. However, focal amplifications—a common mechanism of oncogene activation in human cancers¹—have so far resisted efforts to model them in primary cells or *in vivo*. Although approaches relying on the ectopic expression of individual oncogenes by means of transgenes are useful for modelling transcriptional activation, they fail to reproduce the complexity, intratumoural heterogeneity and evolution of naturally occurring gene amplifications.

Two main classes of amplification have been described: chromosomal and non-chromosomal. The latter are characterized by the presence of multiple copies of circular DNAs that are thought to originate

from the fragmentation and subsequent circularization of segments of chromosomes^{3,4}. These large (0.5–3.0 Mbp) extrachromosomal DNAs (ecDNAs) are also known as ‘double minutes’ owing to their paired appearance in metaphase spreads⁵ (reviewed in refs. 2,6,7). ecDNAs have been detected in several cancer types and are associated with unfavourable prognosis^{8,9}. At least two dozen oncogenes have been reported in circular amplicons, with mouse double minute 2 (*MDM2*) and cellular myelocytomatosis (*MYC*) among the most common⁸. A distinguishing feature of ecDNAs is the absence of centromeres, which results in their random segregation at mitosis^{10–12}. This enables rapid accumulation of large numbers of ecDNAs, promotes intratumoural heterogeneity and facilitates tumour evolution^{8,13,14}. Genes residing on ecDNAs are also transcribed more efficiently than those residing on a linear chromosome, probably owing to a more accessible chromatin configuration, a lack of higher-order compaction^{15,16} and the co-option of DNA regulatory elements that are active in the relevant

¹Cancer Biology and Genetics Program, Memorial Sloan Kettering Cancer Center, New York, NY, USA. ²Department of Radiation Oncology, Memorial Sloan Kettering Cancer Center, New York, NY, USA. ³Louis V. Gerstner Graduate School of Biomedical Sciences, Memorial Sloan Kettering Cancer Center, New York, NY, USA. ⁴BCMB Allied program, Weill Cornell Medicine Graduate School for Medical Sciences, New York, NY, USA. ⁵Center for Stem Cell Biology and Developmental Biology Program, Memorial Sloan Kettering Cancer Center, New York, NY, USA. ⁶Computer Science and Engineering, UC San Diego, La Jolla, CA, USA. ⁷Center for Personal Dynamic Regulomes, Stanford University, Stanford, CA, USA. ⁸Department of Dermatology and Genetics, Stanford University School of Medicine, Stanford, CA, USA. ⁹Department of Pathology, Stanford University School of Medicine, Stanford, CA, USA. ¹⁰Sarafan ChEM-H, Stanford University, Stanford, CA, USA. ¹¹Tri-Institutional MD-PhD Program, Weill Cornell Medicine, Rockefeller University, Memorial Sloan Kettering Cancer Center, New York, NY, USA. ¹²Lewis-Sigler Institute for Integrative Genomics and Department of Computer Science, Princeton University, Princeton, NJ, USA. ¹³Department of Pathology and Laboratory Medicine, Memorial Sloan Kettering Cancer Center, New York, NY, USA. ¹⁴Howard Hughes Medical Institute, Stanford University School of Medicine, Stanford, CA, USA. ¹⁵Halicioglu Data Science Institute, UC San Diego, La Jolla, CA, USA. ¹⁶These authors contributed equally: Davide Pradella, Minsi Zhang, Rui Gao, Melissa A. Yao. ✉e-mail: venturaa@mskcc.org

Article

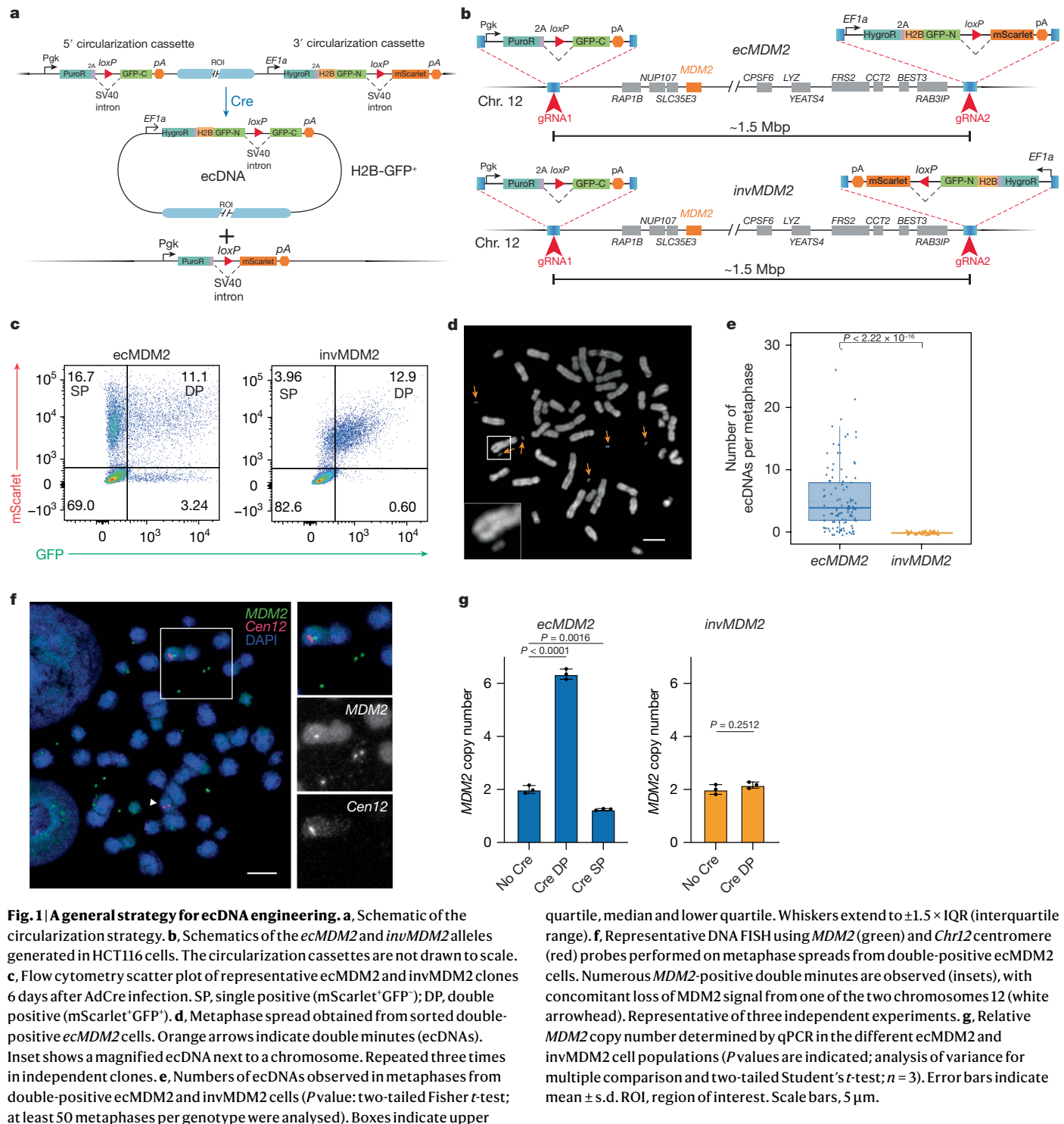


Fig. 1 | A general strategy for ecDNA engineering. **a**, Schematic of the circularization strategy. **b**, Schematics of the *ecMDM2* and *invMDM2* alleles generated in HCT116 cells. The circularization cassettes are not drawn to scale. **c**, Flow cytometry scatter plot of representative *ecMDM2* and *invMDM2* clones 6 days after AdCre infection. SP, single positive (mScarlet+GFP⁻); DP, double positive (mScarlet+GFP⁺). **d**, Metaphase spread obtained from sorted double-positive *ecMDM2* cells. Orange arrows indicate double minutes (ecDNAs). Inset shows a magnified ecDNA next to a chromosome. Repeated three times in independent clones. **e**, Numbers of ecDNAs observed in metaphases from double-positive *ecMDM2* and *invMDM2* cells (*P* value: two-tailed Fisher *t*-test; at least 50 metaphases per genotype were analysed). Boxes indicate upper

quartile, median and lower quartile. Whiskers extend to $\pm 1.5 \times$ IQR (interquartile range). **f**, Representative DNA FISH using *MDM2* (green) and *Cen12* centromere (red) probes performed on metaphase spreads from double-positive *ecMDM2* cells. Numerous *MDM2*-positive double minutes are observed (insets), with concomitant loss of *MDM2* signal from one of the two chromosomes 12 (white arrowhead). Representative of three independent experiments. **g**, Relative *MDM2* copy number determined by qPCR in the different *ecMDM2* and *invMDM2* cell populations (*P* values are indicated; analysis of variance for multiple comparison and two-tailed Student's *t*-test; *n* = 3). Error bars indicate mean \pm s.d. ROI, region of interest. Scale bars, 5 μ m.

cell of origin¹⁷. Finally, ecDNAs can act as mobile enhancers, regulating gene expression in *trans*^{11,18}.

Despite these advances, several fundamental questions remain unresolved. For example, although recent studies have demonstrated the presence of ecDNAs in precancerous oesophageal lesions¹⁹, the precise roles of ecDNAs in tumour initiation and progression, as well as their interactions with the host immune system, remain poorly understood. It is also unknown whether normal cells possess mechanisms to protect against the formation or propagation of ecDNAs, and whether the presence of ecDNAs confers therapeutically actionable vulnerabilities. Progress in this field has been hampered by current limitations in our

ability to precisely engineer focal amplifications. Here we report a strategy to induce and track the formation of specific ecDNAs in primary cells and whole organisms and apply it to engineer the formation of oncogene-containing ecDNAs in cells and mice.

An inducible system to engineer ecDNAs

To engineer ecDNAs analogous in size and behaviour to those found in human cancers, we leveraged the ability of the Cre recombinase to excise and circularize any region flanked by two *loxP* sites with the same orientation^{20,21}. We designed two ‘circularization cassettes’ to

be inserted in *cis* at the desired circularization breakpoints (Fig. 1a). Cre-mediated recombination between the two *loxP*sites contained in the cassettes circularizes the intervening genomic region and reconstitutes a functional H2B–GFP transgene that is encoded by the resulting ecDNA (Fig. 1a). The 3' cassette contains a second fluorescence marker (mScarlet) whose expression is also induced upon recombination but remains linked to the linear chromosome. This dual colour system allows tracking of cells harbouring the engineered ecDNAs and discriminates between cells that have undergone circularization but have subsequently lost the ecDNA(s) owing to random segregation ($\text{GFP}^+ \text{mScarlet}^+$) (Extended Data Fig. 1a) and cells harbouring a tandem duplication caused by Cre-mediated recombination between sister chromatids ($\text{GFP}^+ \text{mScarlet}^+$).

As a proof of concept for this strategy, we chose the HCT116 colorectal cancer cell line, because it is near-diploid and chromosomally stable and harbours no ecDNAs²². Using CRISPR–Cas9-mediated genome editing, we inserted two cassettes flanking a 1.5 Mbp region on chromosome 12. This region is recurrently amplified in human cancers^{23–25} and includes the human *MDM2* oncogene (Fig. 1b), a key negative regulator of the p53 pathway^{26,27}. As a control, we generated a companion HCT116 line in which the orientation of the 3' cassette was flipped, so that the two *loxP*sites were in the opposite orientation (Fig. 1b). With this configuration, the genomic region flanked by the cassettes was inverted rather than excised upon Cre expression and therefore, both fluorescent reporters remained linked to the linear chromosome (Extended Data Fig. 1b). We refer to these two engineered cell lines as ecMDM2 and invMDM2, respectively.

Cells expressing both GFP and mScarlet (double positive) were readily detected in both invMDM2 and ecMDM2 clones infected with Cre-expressing recombinant adenoviruses (AdCre) (Fig. 1c; gating strategy and gel source data for all figures are provided in Supplementary Fig. 1). As predicted, in ecMDM2 clones, we also observed a large fraction of cells expressing mScarlet but not GFP (single positive), as well as a much smaller population of cells expressing GFP but not mScarlet (Fig. 1c). The presence of single-positive cells was consistent with loss of ecDNAs, whereas the small population of $\text{GFP}^+ \text{mScarlet}^-$ ecMDM2 cells was probably a product of Cre-mediated recombination between *loxP*sites on sister chromatids, which is predicted to lead to tandem duplication.

To confirm that concomitant mScarlet and GFP expression in ecMDM2 cells reflected the presence of engineered ecDNAs, we generated metaphase spreads from sorted double-positive ecMDM2 and invMDM2 cells. Most metaphases from ecMDM2 cells—but none from invMDM2 cells—contained *MDM2*-positive ecDNAs. As expected, loss of *MDM2* signal from one of the two copies of chromosome 12 was observed in metaphases from ecMDM2 cells (89 of 91, 98% of metaphases examined; Fig. 1d–f). Genomic quantitative PCR (qPCR) confirmed amplification of the *MDM2* locus in double-positive ecMDM2 cells as well as loss of one copy of *MDM2* in the single-positive population, whereas *MDM2* copy number was unchanged in double-positive invMDM2 cells (Fig. 1g). Notably, the variance in GFP expression within the double-positive population was substantially greater in ecMDM2 cells compared with invMDM2 cells, reflecting the diversity in ecDNA copy number caused by random segregation at mitosis (Extended Data Fig. 1c,d).

Tracking ecDNA dynamics in cells

To assess whether GFP expression could be used to track ecDNA abundance, we sorted AdCre-infected ecMDM2 cells into four bins on the basis of GFP expression (Fig. 2a). As shown in Fig. 2b, the average number of ecDNAs per metaphase was positively correlated with GFP intensity, and shallow whole-genome sequencing (sWGS) identified a corresponding focal amplification precisely spanning the 1.5 Mbp region demarcated by the two circularization cassettes (Fig. 2c).

As expected, no amplification of this region was present in double-positive invMDM2 cells (Fig. 2c).

Having established that GFP intensity could be used as a semiquantitative surrogate for ecDNA abundance, we then examined the dynamics of the engineered ecDNAs in HCT116 cells. We infected ecMDM2 and invMDM2 cells with AdCre and measured the fraction of double-positive and single-positive cells at different time points. For both ecMDM2 and invMDM2 cells, the fraction of double-positive cells peaked approximately 5–6 days postinfection (Extended Data Fig. 2a). However, whereas the double-positive population of invMDM2 cells remained constant throughout the rest of the experiment, that of ecMDM2 cells progressively decreased, accompanied by a corresponding increase in the fraction of single-positive ($\text{GFP}^+ \text{mScarlet}^+$) cells. To test whether the single-positive cells derived from initially double-positive cells, we first sorted double-positive ecMDM2 and invMDM2 cells. Upon serial passage, ecMDM2 cells gradually lost GFP expression, becoming single positive, whereas invMDM2 cells remained uniformly double positive (Fig. 2d,e). This result indicates that the engineered ecDNAs are gradually lost in HCT116 cells, probably because extra copies of the genes on the amplicon do not provide a fitness advantage to these cancer cells *in vitro*¹⁴. If this interpretation is correct, providing an artificial selective pressure should be sufficient to promote accumulation of the engineered ecDNAs. To test this hypothesis, we leveraged the hygromycin resistance gene encoded by the engineered ecDNAs (Fig. 1a and Extended Data Fig. 1a). When double-positive ecMDM2 cells were cultured in the presence of increasing concentrations of hygromycin (0–5 mg ml^{−1}), we observed a corresponding increase in GFP intensity in the population (Fig. 2f and Extended Data Fig. 2b), accompanied by progressive accumulation of *MDM2*-containing ecDNAs (Fig. 2g and Extended Data Fig. 2c) and an increase in *MDM2* copy number (Fig. 2h).

While analysing the results of these experiments, we also noticed labelling of homogeneously staining regions instead of ecDNAs by the *MDM2* probe in approximately 6% (6 of 91) of metaphases generated from sorted double-positive ecMDM2 cells (Extended Data Fig. 2d). In all cases, one of the two chromosomes 12 showed loss of endogenous *MDM2* staining, confirming that these cells had previously circularized and excised the *ecMDM2* allele. This indicates that the engineered ecDNAs can occasionally reintegrate into a different chromosome, a poorly understood phenomenon that has been reported for naturally occurring ecDNAs^{3,4,28}.

Generation of mice with inducible ecDNAs

We next generated genetically engineered mice harbouring *loxP*sites spanning a 1.7 Mbp genomic region on chromosome 15 that contained, among other genes, the *Myc* locus (Fig. 3a and Extended Data Fig. 3a). This engineered allele will be referred to hereafter as *Myc*^{ec}. *Myc*^{ec/+} and *Myc*^{ec/ec} mice were obtained at Mendelian frequency, were viable and fertile, had no obvious phenotype (Extended Data Fig. 3b–d) and showed excision and circularization of the region flanked by the *loxP* sites upon Cre expression (Extended Data Fig. 3e,f).

To determine whether the engineered ecDNAs could form and accumulate in primary cells, we isolated adult neural stem cells (aNSCs) from *Myc*^{ec/+} *p53*^{fl/fl} mice and *p53*^{fl/fl} littermate control mice and infected them with AdCre. Following infection, these cells were propagated *in vitro* and evaluated weekly for the presence of ecDNAs (Fig. 3b). Initially, only a small fraction of *Myc*^{ec/+} *p53*^{fl/fl} aNSCs contained ecDNAs, but the number of metaphases with ecDNAs and the number of ecDNAs per metaphase increased markedly over the ensuing weeks, such that by week 5, every metaphase contained multiple *Myc*-positive ecDNAs (Fig. 3c–e). Detection of a circular amplicon exactly matching the region flanked by the *loxP*sites and reaching an average of around 135 copies per cell by week 5 further corroborated these findings (Fig. 3f and Extended Data Fig. 4a). Notably, in interphase nuclei, the *Myc* DNA fluorescence *in situ* hybridization (FISH) signal was often localized into

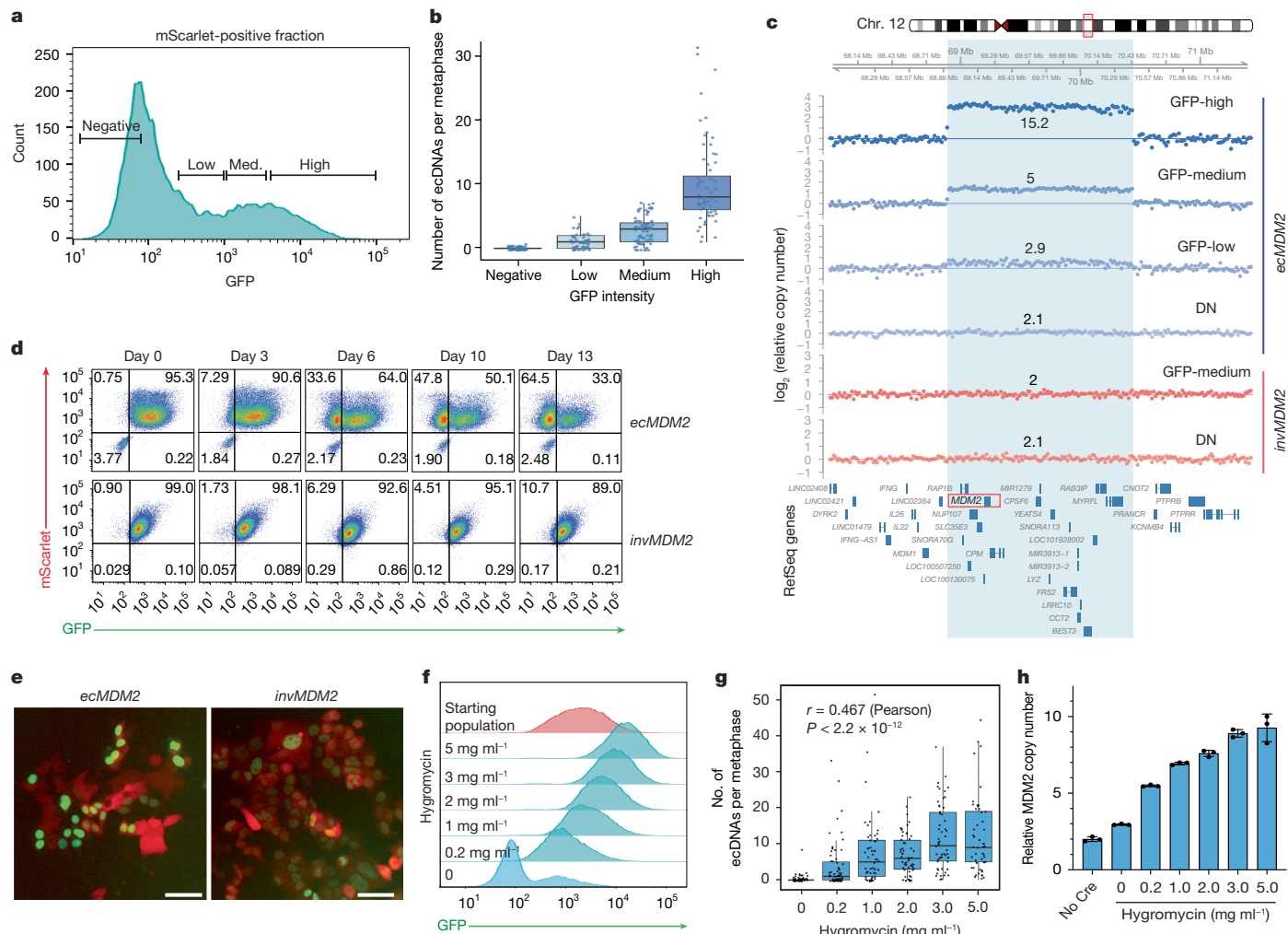


Fig. 2 | Dynamics of engineered ecDNAs in HCT116 cells. **a**, Double-positive cells from an AdCre-infected ecMDM2 line were cultured in the absence of hygromycin and sorted into four bins on the basis of GFP intensity (negative, low, medium (med.) and high) as indicated. **b**, Box-and-whiskers plot showing the number of ecDNAs per metaphase in each bin. Box plot represents upper quartile, median and lower quartile. Whiskers extending to $\pm 1.5 \times$ IQR are shown ($n = 60, 57, 78$ and 68 metaphases). **c**, ecMDM2 and invMDM2 cells were infected with AdCre, sorted according to mScarlet and GFP intensity, and analysed by SWGS. The panel shows the \log_2 ratio of relative copy number, as inferred from quantitative DNA sequencing (QDNAseq) analysis, across the region of chromosome 12 surrounding the expected ecDNA (defined by the light blue highlight). The number above each track indicates the amplicon copy number. **d**, Sorted double-positive cells from AdCre-infected ecMDM2 and

invMDM2 clones were cultured in the absence of hygromycin and analysed by flow cytometry at the indicated time points. **e**, mScarlet and GFP expression in double-positive sorted ecMDM2 (left) and invMDM2 (right) cells maintained in media without hygromycin for 1 week. Independently repeated twice. **f**, Histogram plot of GFP fluorescence. AdCre-infected and sorted double-positive ecMDM2 cells were expanded for 13 days in medium containing the indicated concentration of hygromycin and analysed by flow cytometry. **g**, Box-and-whiskers plot showing the number of ecDNAs per metaphase observed in the cells described in **e**. Boxes indicate upper quartile, median and lower quartile. Whiskers extend to $\pm 1.5 \times$ IQR. Pearson correlation coefficients and associated P values are shown ($n = 58, 65, 56, 56, 54$ and 51 metaphases). **h**, MDM2 copy number as determined by genomic qPCR on cells from **f**. Error bars indicate mean \pm s.d. $n = 3$ technical replicates. Scale bars, $50 \mu\text{m}$.

discrete clusters, rather than being randomly distributed (Fig. 3e and Extended Data Fig. 4b), reminiscent of the ‘enhancer hubs’ previously described for naturally occurring MYC-containing ecDNAs^{11,15,18}.

To define the transcriptional status of the engineered ecDNAs, we performed assay for transposase-accessible chromatin with sequencing (ATAC-seq) and RNA sequencing (RNA-seq) analyses of *p53^{R/R}* and *Myc^{ec/+} p53^{R/R}* aNSCs at 5 weeks after AdCre infection (Supplementary Table 1). ATAC-seq indicated that the chromatin on the engineered ecDNAs was largely open or mononucleosomal (Extended Data Fig. 4c,d). After normalization for copy number, the region on the ecDNAs contained slightly more ATAC-seq reads than the same region on the linear chromosome (Extended Data Fig. 4e). Accordingly, all genes included in the amplicon were upregulated, albeit to different extents (Fig. 3g and Extended Data Fig. 4f–h), and gene set enrichment analysis showed strong activation of MYC targets (Fig. 3h,i). In analogous experiments,

we detected spontaneous accumulation of the engineered ecDNAs upon Cre expression in three further primary cell types derived from these mice: cerebellar progenitors, mouse embryonic fibroblasts (MEFs) and hepatocytes (Extended Data Fig. 5).

These results demonstrate the generation of a targeted focal oncogene amplification mediated by replication-competent and transcriptionally active engineered ecDNAs in several primary cell types.

ecDNAs immortalize primary cells

To investigate the oncogenic potential of engineered ecDNAs, we generated a second mouse strain containing *loxP* sites flanking a 1.3 Mb segment on chromosome 10 (*Mdm2^{ec}*, Fig. 4a and Extended Data Fig. 6a–c). This region contains, among other genes, the *Mdm2* oncogene and is syntenic to a region recurrently amplified in ecDNAs in human cancers.

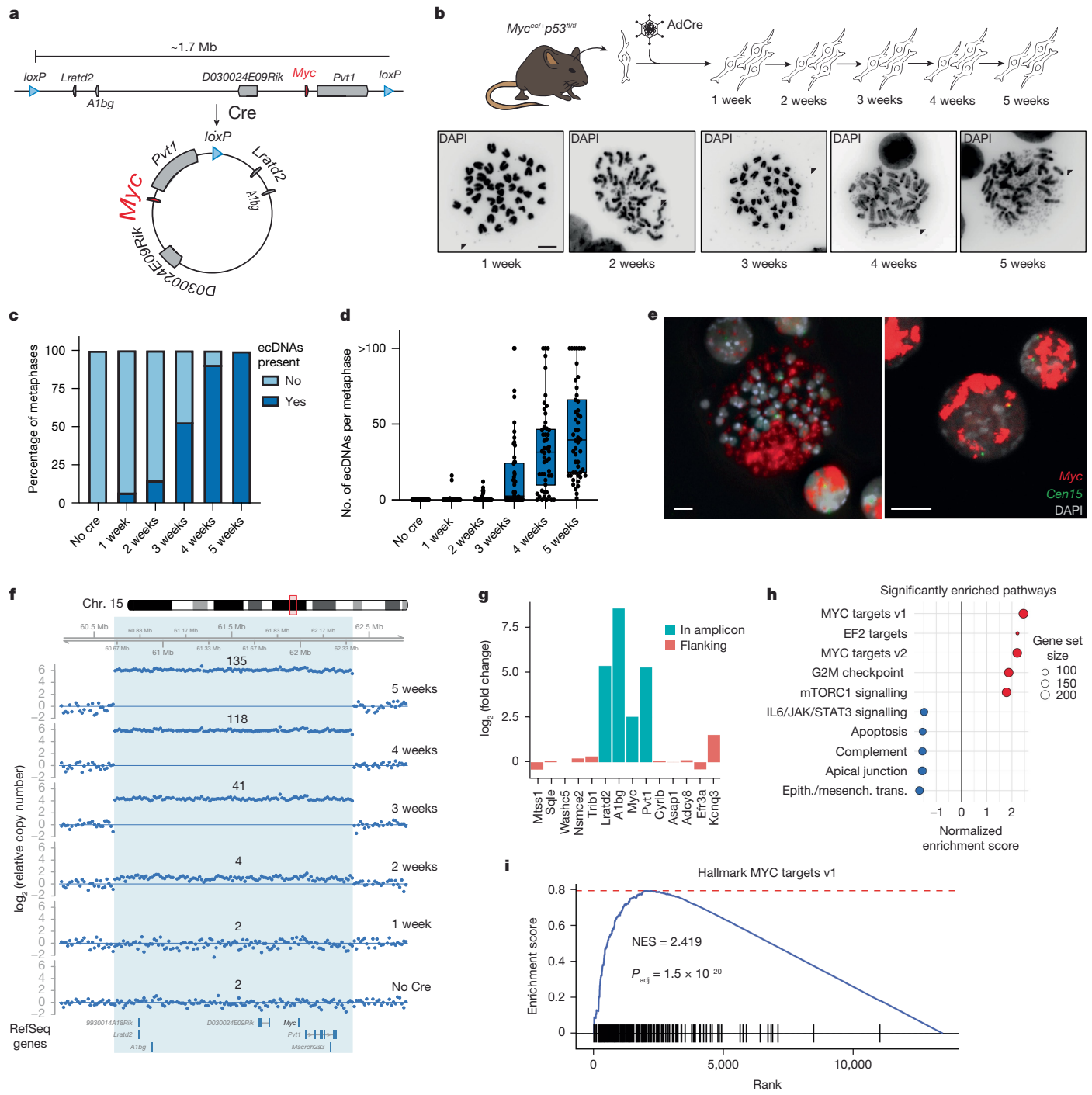


Fig. 3 | Generation of Myc-containing ecDNAs in primary cells from genetically engineered mice. **a**, Schematic of the *Myc*^{ec} allele. **b**, aNSCs derived from *Myc*^{ec}/*p53*^{fl/fl} mice were infected with AdCre and propagated in vitro for 5 weeks. Metaphase spreads (lower panels) at different time points were collected, and representative micrographs are shown. Arrowheads indicate double minutes (ecDNAs). **c**, Bar plot showing the fraction of metaphases with or without ecDNAs. **d**, Box-and-whiskers plot showing the number of ecDNA per metaphase in *Myc*^{ec}/*p53*^{fl/fl} aNSC at different times upon AdCre infection. $n = 50$ metaphases analysed per condition. Boxes indicate upper quartile, median and lower quartile. Whiskers extend to $\pm 1.5 \times$ IQR. **e**, Metaphase (left) and interphase FISH (right) performed on aNSCs from *Myc*^{ec}/*p53*^{fl/fl} 5 weeks after AdCre infection. The Myc signal is shown in red, and a probe labelling a pericentromeric region of chromosome 15 is shown in green. Representative of two independent experiments. **f**, sWGS analysis of *Myc*^{ec}/*p53*^{fl/fl} aNSCs at

different time points after AdCre infection. The panel shows relative copy number, as inferred from QDNaseq analysis, across the region of chromosome 15 surrounding the predicted Myc-containing ecDNA (light blue). Notice the progressive increase in copy number of a focal amplification matching the predicted ecDNA boundaries. **g**, \log_2 fold change of mRNA expression of genes included in (blue) or flanking (red) the engineered Myc amplicon in *Myc*^{ec}/*p53*^{fl/fl} versus *p53*^{fl/fl} aNSCs 5 weeks after AdCre infection, as determined by RNA-seq analysis. **h**, Gene set enrichment analysis showing the top enriched hallmark pathways in *Myc*^{ec}/*p53*^{fl/fl} versus *p53*^{fl/fl} aNSCs at 5 weeks after AdCre infection. **i**, Gene set enrichment plot of hallmark gene set MYC Targets v1, the most enriched gene set in *Myc*^{ec}/*p53*^{fl/fl} aNSCs. NES, normalized enrichment score; P_{adj} , adjusted P value. NES and P_{adj} were calculated as per the fgsea package in R. Scale bars, 5 μ m.

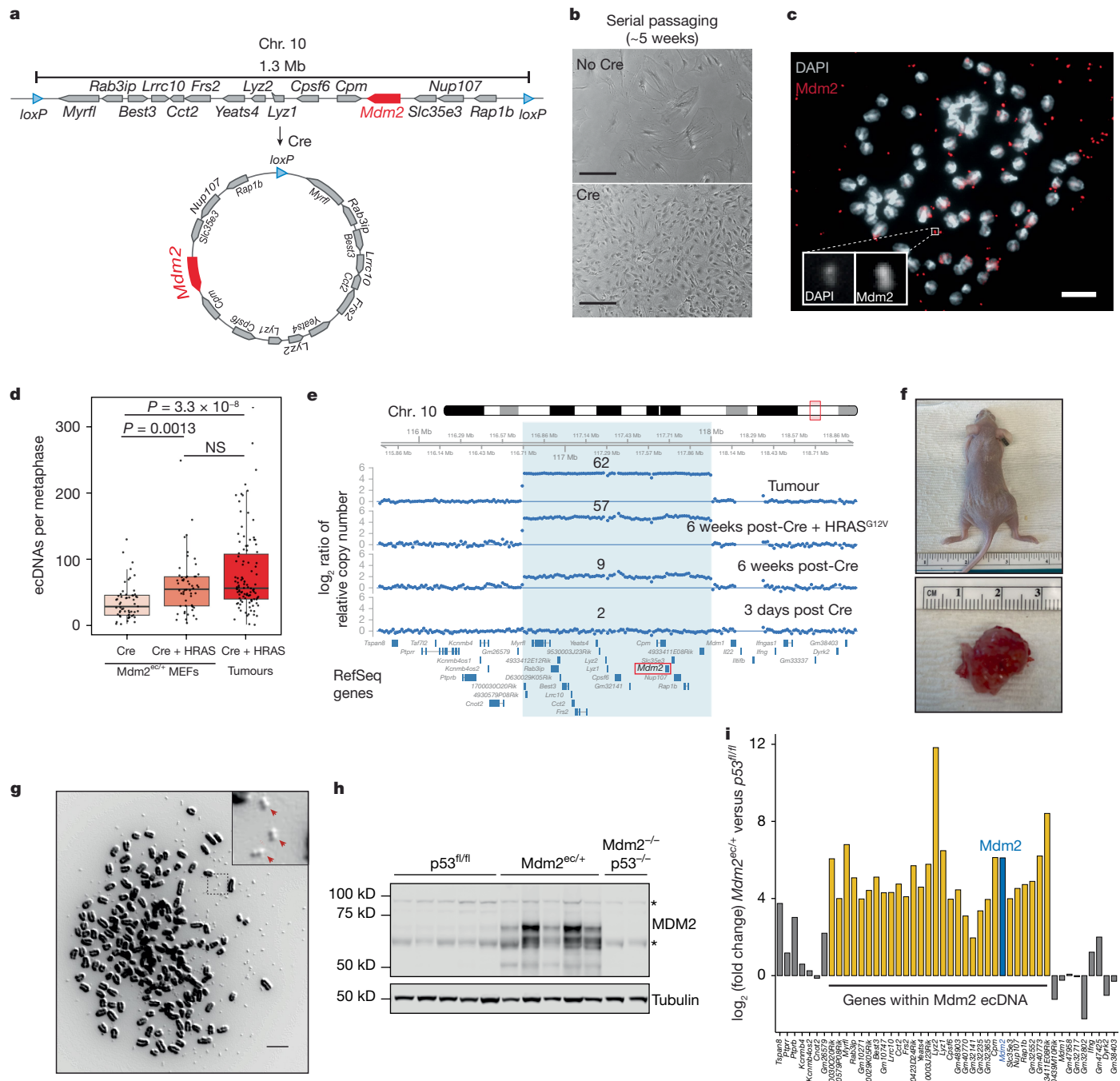


Fig. 4 | Engineered Mdm2-containing ecDNAs promote immortalization and transformation of primary mouse cells. **a**, Schematic of the *Mdm2*^{ec} allele. **b**, *Mdm2*^{ec/+} MEFs approximately 5 weeks after being infected with AdCre or left untreated. Repeated on three independent MEF lines. **c**, Metaphase spread and DNA FISH showing the presence of multiple *Mdm2*-positive ecDNAs in AdCre-infected *Mdm2*^{ec/+} MEFs (inset). Repeated twice. **d**, Number of ecDNAs per metaphase in AdCre-infected *Mdm2*^{ec/+} MEFs transduced or not with *HRAS*^{G12V} and in tumours ($n = 4$) derived from injecting the transduced cells into the flanks of nude mice. Boxes indicate upper quartile, median and lower quartile. Whiskers extend to $\pm 1.5 \times$ IQR. P values, pairwise Wilcoxon rank-sum test corrected for multiple testing. $n = 57, 54$ and 106 metaphases. **e**, sWGS analysis of AdCre-infected *Mdm2*^{ec/+} MEFs at the indicated time points after AdCre infection showing progressive accumulation of the *Mdm2* ecDNA over time. ‘Tumour’ indicates sWGS of a tumour obtained by injecting the

HRAS-infected cells into the flank of a nude mouse. The absence of signal in the region immediately downstream of the amplicon is due to QDNASeq ignoring low-mappability regions. Amplicon copy number is indicated above each track. **f**, Representative image of a tumour developing in a nude mouse injected subcutaneously with AdCre- and *HRAS*^{G12V}-infected *Mdm2*^{ec/+} MEFs. **g**, Metaphase spread showing numerous ecDNAs (arrows) in cells isolated from the tumour shown in **f**. **h**, MDM2 immunoblot of lysates from tumours generated as indicated above. Mdm2-p53 double-knockout tumours served as negative controls for the MDM2 antibody. Asterisks indicate non-specific bands. Repeated on three independent tumours. **i**, Bar plot showing the \log_2 fold change of genes included within the *Mdm2* amplicon (light orange) and immediately flanking it (grey) in Cre-treated *Mdm2*^{ec/+} *HRAS*^{G12V} versus *p53*^{fl/fl} *HRAS*^{G12V} MEFs as determined by RNA-seq. *Mdm2* is highlighted in blue. Scale bars, $350 \mu\text{m}$ (**b**), $10 \mu\text{m}$ (**c,g**).

Mdm2^{ec/+} and *Mdm2*^{ec/ec} mice are viable and fertile and do not show any obvious abnormality (Extended Data Fig. 6d,e and data not shown).

We next examined whether Cre-mediated induction of ecDNAs containing the *Mdm2* locus could lead to *Mdm2* amplification and suppression of the p53 pathway in primary cells. Freshly isolated *Mdm2*^{ec/+} and wild-type MEFs were either left untreated or infected with AdCre (Extended Data Fig. 6f,g). As expected, untreated *Mdm2*^{ec/+} and wild-type MEFs stopped proliferating after approximately 3–4 weeks in culture and acquired the characteristic morphology of senescent cells (Fig. 4b). By contrast, AdCre-infected *Mdm2*^{ec/+} MEFs became immortalized, accumulated ecDNAs containing the *Mdm2* locus (Fig. 4c,d) and showed strong upregulation of *Mdm2* RNA and protein expression (Extended Data Fig. 7a,b). sWGS of these cells confirmed the presence of a circular focal gene amplification matching the region flanked by the two *loxP* sites (Fig. 4e and Extended Data Fig. 7c). Inactivation of the p53 pathway is also required for the transformation of MEFs by ectopically expressed oncogenic HRAS^{G12V29}. We transduced early passage wild-type and Cre-treated *Mdm2*^{ec/+} MEFs with retroviruses encoding the HRAS^{G12V} oncogene. Control cells became senescent after an initial burst of proliferation, whereas AdCre-infected *Mdm2*^{ec/+} cells continued proliferating and formed tumours when injected into immunocompromised mice (all seven mice, two independent MEF lines, Fig. 4f). No tumours developed in the five mice injected with HRAS^{G12V}-transduced wild-type MEFs or in the four mice injected with HRAS^{G12V}-transduced *Mdm2*^{ec/+} MEFs that had not been previously infected with AdCre.

The resulting tumours were characterized by marked circular amplification of the region flanked by the *loxP* sites (Fig. 4e) and contained on average approximately 60 *Mdm2* ecDNAs per cell (Fig. 4d,e,g). The circular amplicons were characterized by open chromatin and drove increased expression of *Mdm2* and the other genes they contained (Fig. 4h,i, Extended Data Fig. 8a–d and Supplementary Table 2), indicating that the engineered ecDNAs were transcriptionally active and could propagate in vivo. Histologically, the tumours had a high-grade phenotype, with spindle and pleomorphic cells arranged in short fascicles, showing infiltrative growth within skeletal muscle (Extended Data Fig. 8e–h). The tumour showed a high mitotic count and in areas showed single or multi-intracytoplasmic fat vacuoles with focal nuclear indentation, a characteristic feature of lipoblasts. The alternating high-grade undifferentiated component with areas with adipocytic differentiation closely resembled the features of dedifferentiated liposarcoma, a tumour whose genetic hallmark is the amplification of *MDM2* (ref. 30).

To verify the causative role of *Mdm2* amplification in the immortalization and transformation of these cells, we treated them with increasing concentrations of MDM2 antagonist milademetan³¹. This treatment reactivated the p53 pathway and potently inhibited proliferation of the transformed *Mdm2*^{ec/+} cells at nanomolar concentrations, whereas it was largely ineffective against the Cre-treated HRAS-transformed *p53*^{fl/fl} MEFs used as controls (Extended Data Fig. 9a–c).

These results demonstrate that engineered *Mdm2*-containing ecDNAs rapidly and spontaneously accumulate in primary MEFs, promote their immortalization and cooperate with HRAS^{G12V} in inducing oncogenic transformation.

Engineered ecDNAs promote tumorigenesis

ecDNAs are frequently detected in advanced human cancers, but their contribution to tumour initiation and progression remains a key unanswered question. To assess whether the engineered ecDNAs could contribute to tumorigenesis in an autochthonous context, we induced widespread circularization of the *Mdm2*^{ec} allele directly in vivo by crossing *Actin-Cre*³² and *Mdm2*^{ec/+} mice (Extended Data Fig. 10a). We then leveraged the fact that in mice, MYC-driven hepatocellular carcinoma requires a second genetic event, such as inactivation of the p53 pathway^{33,34}, and reasoned that this could be achieved by *Mdm2* amplification through engineered ecDNAs. We delivered a MYC transgene to

the livers of adult *Actin-Cre Mdm2*^{ec/+} and control (*Actin-Cre*) mice by hydrodynamic tail-vein injection (Fig. 5a). Although none of the control animals (*n* = 6) developed tumours, three of the six *Actin-Cre Mdm2*^{ec/+} mice developed multiple liver tumours within 6–18 weeks postinjection (Fig. 5b).

The tumours had features of poorly differentiated hepatocellular carcinomas, characterized by broadly expanded trabeculae surrounded by endothelial cells, frequent mitoses and apoptotic figures (Fig. 5c and Extended Data Fig. 10b). Immunostaining showed strong expression of hepatocyte nuclear factor 4 alpha (HNF4α) and lack of expression of cytokeratin 19 (Fig. 5d and Extended Data Fig. 10c). Crucially, metaphase spreads obtained from freshly dissociated tumour cells showed the presence of dozens of *Mdm2*-positive ecDNAs (Fig. 5e), a result that was confirmed by DNA FISH on tumour sections (Fig. 5f) and was accompanied by strong upregulation of the *Mdm2* messenger RNA (mRNA) (Fig. 5g and Extended Data Fig. 10d). Finally, sWGS and AmpliCon Architect analysis of DNA obtained from various tumours revealed marked focal amplification of the *Mdm2*^{ec} region in all cases, confirming that *Mdm2* amplification had been initiated by Cre-mediated circularization (Fig. 5h and Extended Data Fig. 10e,f).

Together, these results offer direct experimental evidence that engineered ecDNAs can contribute to tumour formation in vivo and validate an autochthonous mouse model of cancer driven by an engineered focal gene amplification.

Discussion

We have described a general strategy to engineer focal gene amplifications mediated by ecDNAs in cells and in mice. To showcase its flexibility, we generated human cancer cell lines with Cre-inducible ecDNAs that can then be tracked using fluorescent reporters encoded by the ecDNAs and the linear chromosome from which they originate. We applied a similar strategy to engineer *Mdm2*- and *Myc*-containing ecDNAs in mice and showed that these ecDNAs confer a fitness advantage on primary cells harbouring them, accumulate over time in vitro, and promote cell proliferation and immortalization. Finally, we demonstrated that engineered *Mdm2*-containing ecDNAs promote the oncogenic transformation of mouse fibroblasts ex vivo when combined with oncogenic RAS and lead to the development of hepatocellular carcinomas when combined with ectopic MYC expression in vivo.

These results have notable biological implications because they demonstrate that oncogene-containing ecDNAs can form and rapidly accumulate in primary non-transformed cells derived from all three embryonic layers. This is relevant because until now, oncogene-containing ecDNAs had been observed only in established cancer cell lines and primary tumours, not in primary cells. Analogously, previous attempts to induce the formation of ecDNAs using CRISPR–Cas9 (refs. 14,35) or through drug selection^{4,36} had been performed in cancer cell lines but not in primary cells or whole organisms. It will be important to determine whether all cell types are equally permissive to ecDNA formation and propagation and to systematically explore the impact of gene regulatory elements contained in the engineered ecDNAs on their propagation, accumulation and tissue specificity, as recently suggested by studies in human cancers¹⁷. Equally relevant is the demonstration that engineered *Mdm2* ecDNAs can cooperate with MYC in promoting autochthonous hepatocellular carcinomas in mice. This result provides direct experimental evidence that oncogene-containing ecDNAs can contribute to tumour progression in vivo and paves the way for future studies exploring the role of the immune system in the development and maintenance of ecDNA-driven tumours.

Besides the biological insights gained in this study, we expect that the general strategy we have developed and the reagents we have generated will prove useful in dissecting various aspects of ecDNA biology that are unresolved at present. For example, the presence of selectable markers and fluorescence reporters in the engineered ecDNAs make them

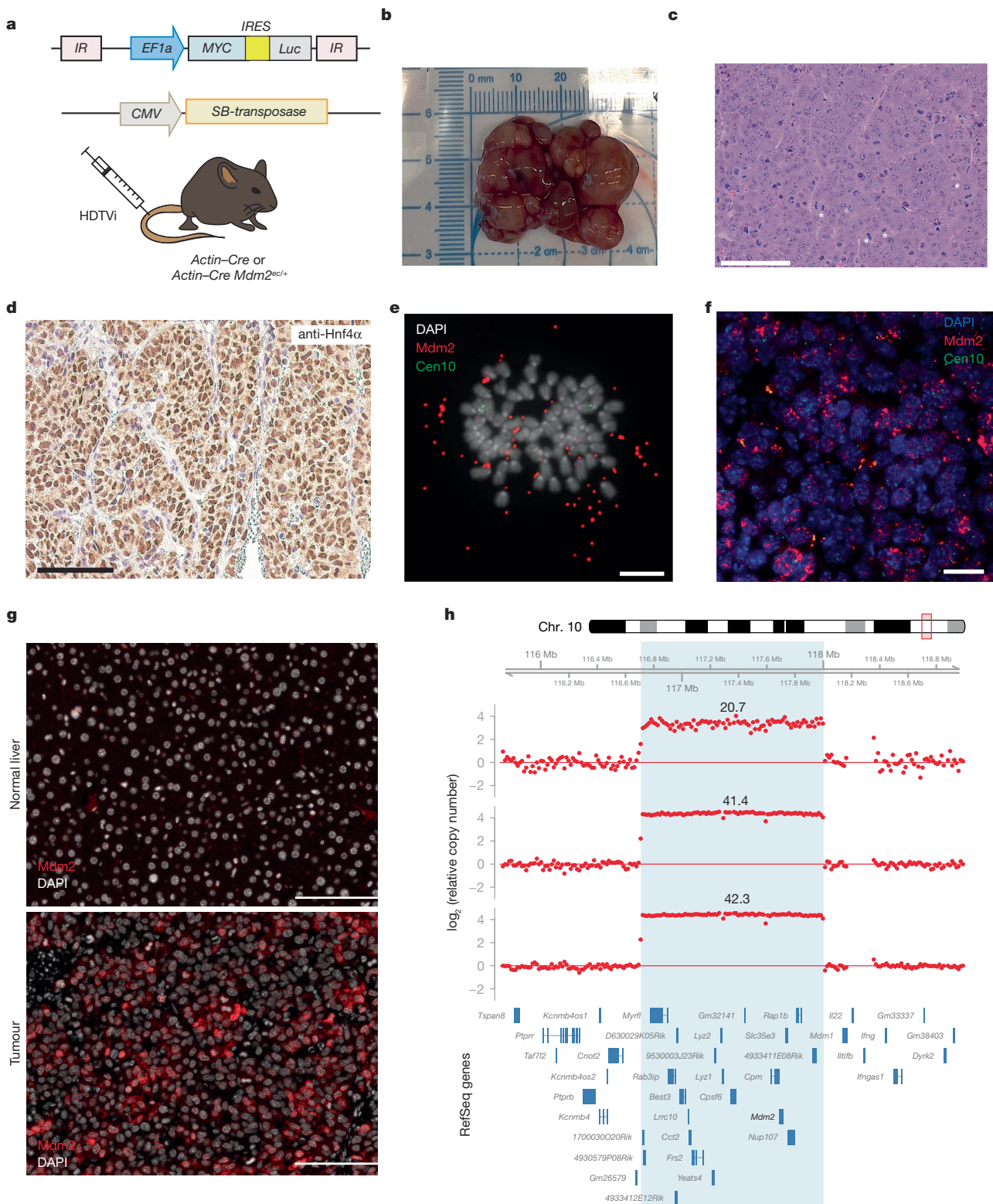


Fig. 5 | An autochthonous mouse model of cancer harbouring engineered ecDNAs. **a**, Schematics of the experimental strategy. A MYC-IRES-luciferase-encoding transposon and the Sleeping Beauty transposase were delivered by hydrodynamic tail-vein injection to six *Actin-Cre Mdm2*^{ec/+} and six *Actin-Cre* mice. **b**, Macroscopic appearance of the liver of a MYC-injected *Actin-Cre Mdm2*^{ec/+} mouse showing multiple nodules. **c,d**, Representative haematoxylin and eosin staining (**c**) and anti-*Hnf4α* immunostaining (**d**) of a liver lesion arising in *Actin-Cre Mdm2*^{ec/+} mouse. Arrowheads in **d** point to mitotic figures. Representative of eight tumour nodules in three mice. **e**, Metaphase spreads of cells obtained from a dissociated liver tumour showing multiple double-minute

chromosomes (left panel) containing the *Mdm2* locus (DNA FISH, right panel). Representative of three independent experiments **f**, DNA FISH on a tumour section using an *Mdm2*-specific probe showing amplification of the *Mdm2* locus. **g**, Sections of normal liver and of a tumour nodule were stained by RNA FISH using a probe specific to the *Mdm2*mRNA. A marked increase in *Mdm2* signal (red) is evident in the tumour section. Repeated on three independent tumours. **h**, sWGS analysis of tumours from three mice, showing the presence of a focal amplification spanning the *Mdm2*^{ec} region (blue shaded area). The computed average copy number of the amplicon is indicated on top of each track. Scale bars, 100 μm (**c,d,g**), 10 μm (**e**), 20 μm (**f**).

ideally suited to use in large-scale screens to identify factors that are required for ecDNA propagation and maintenance and unique vulnerabilities conferred on cancer cells by the presence of ecDNAs. The ability to engineer ecDNAs in primary cells will also facilitate investigation of the mechanisms underlying chromatin changes that have been recently described in cancer-associated ecDNAs and the role of DNA regulatory elements present in human ecDNAs that have been proposed to affect gene expression in *trans*^{11,18}. We note that although in the present study we used the Cre–*lox* system to induce circularization, the same results can be achieved using other site-specific recombinases (FlpO or Dre)³⁷, further expanding the potential applications of this strategy to model tumour evolution *in vivo*.

Despite these benefits, the approach described here has some limitations. First, although our strategy recapitulates the subset of ecDNAs generated by two double-stranded DNA breaks followed by recircularization, ecDNAs can also result from chromothripsis⁴, for which Cre-induced recombination is not an accurate proxy. Second, the efficiency of Cre-induced circularization is known to decrease as the distance between the *loxP*sites increases. For the ecDNAs generated in this study, we observed an efficiency of recombination of 7–25% upon a single Cre pulse in cells and up to 80% *in vivo* using constitutive Cre expression. Although the size of the ecDNAs we have engineered (approximately 1.3–1.7 Mbp) is well within the range of many naturally occurring ecDNAs, it is likely that the circularization efficiency will be lower when attempting to model larger ecDNAs (3 Mbp or more) or when temporally restricting Cre expression. Third, for the *in vitro* experiments, we used H2B–GFP as a reporter for the presence of ecDNAs. Although H2B–GFP has the advantage of labelling the chromatin, allowing direct visualization of ecDNAs during mitosis, GFP variants with shorter half-lives may be better suited to the study of ecDNA dynamics in cell populations and may better facilitate pooled CRISPR screens.

Of note, we have not yet observed the development of autochthonous tumours harbouring amplified *Myc*-containing ecDNAs in *Myc*^{ec/+} mice in tissues where MYC overexpression readily induces tumour formation, even upon concomitant p53 inactivation (Supplementary Table 3). This cannot be explained by poor Cre-mediated circularization of the *Myc*^{ec} allele *in vivo* (Extended Data Fig. 3e,f), or by an inability of the *Myc*-containing ecDNAs to propagate, as they readily accumulated *in vitro* in several cell types upon Cre expression (Fig. 3 and Extended Data Fig. 5). This resistance to tumour formation upon engineered *Myc* amplification might be in part related to a previously described negative autoregulatory feedback loop whereby ectopic MYC expression strongly represses transcription of the endogenous *MYC* gene in non-transformed cells^{38–40}. This autoregulatory loop could serve as a tumour suppressive barrier, moderating MYC expression despite increased *MYC* copy number. Our finding that *Myc* mRNA levels were upregulated less than one would expect on the basis of the observed increase in copy number in aNSC-containing engineered *Myc* ecDNAs (Fig. 3 and Extended Data Fig. 4f) is consistent with this hypothesis.

Finally, it is notable that widespread *in vivo* Mdm2 circularization alone—as seen in *Actin-Cre Mdm2*^{ec/+} mice—did not lead to spontaneous tumour formation. This is in contrast to findings reported in mice harbouring *Mdm2* transgenes⁴¹ or targeted deletion of p53 (refs. 42,43) and could reflect a unique feature of ecDNAs compared with other classes of cancer-associated mutations: the formation of an extrachromosomal copy of an oncogene—either through Cre-mediated engineering or spontaneously—is not per se oncogenic, as gene copy number is not affected by circularization. It is only after multiple rounds of cell division with random segregation and selection that the circular amplicon can exert oncogenic functions. This underappreciated feature of focal oncogene amplifications is likely to have clinical implications and needs to be taken into account in the design of other mouse models of human cancers harbouring ecDNAs. We expect that the tools and

genetically engineered mouse models described here will enable the scientific community to address this and other key questions concerning the biology of ecDNAs and their roles in tumour initiation and tumour progression.

Online content

Any methods, additional references, Nature Portfolio reporting summaries, source data, extended data, supplementary information, acknowledgements, peer review information; details of author contributions and competing interests; and statements of data and code availability are available at <https://doi.org/10.1038/s41586-024-08318-8>.

- Beroukhim, R. et al. The landscape of somatic copy-number alteration across human cancers. *Nature* **463**, 899–905 (2010).
- Yi, E., Chamorro Gonzalez, R., Henssen, A. G. & Verhaak, R. G. W. Extrachromosomal DNA amplifications in cancer. *Nat. Rev. Genet.* **23**, 760–771 (2022).
- Rosswoog, C. et al. Chromothripsis followed by circular recombination drives oncogene amplification in human cancer. *Nat. Genet.* **53**, 1673–1685 (2021).
- Shoshani, O. et al. Chromothripsis drives the evolution of gene amplification in cancer. *Nature* **591**, 137–141 (2021).
- Cox, D., Yuncken, C. & Spriggs, A. I. Minute chromatin bodies in malignant tumours of childhood. *Lancet* **1**, 55–58 (1965).
- Wu, S., Bafna, V., Chang, H. Y. & Mischel, P. S. Extrachromosomal DNA: an emerging hallmark in human cancer. *Annu. Rev. Pathol.* **17**, 367–386 (2022).
- Noer, J. B., Horsdal, O. K., Xiang, X., Luo, Y. & Regenberg, B. Extrachromosomal circular DNA in cancer: history, current knowledge, and methods. *Trends Genet.* **38**, 766–781 (2022).
- Kim, H. et al. Extrachromosomal DNA is associated with oncogene amplification and poor outcome across multiple cancers. *Nat. Genet.* **52**, 891–897 (2020).
- Turner, K. M. et al. Extrachromosomal oncogene amplification drives tumour evolution and genetic heterogeneity. *Nature* **543**, 122–125 (2017).
- deCarvalho, A. C. et al. Discordant inheritance of chromosomal and extrachromosomal DNA elements contributes to dynamic disease evolution in glioblastoma. *Nat. Genet.* **50**, 708–717 (2018).
- Zhu, Y. et al. Oncogenic extrachromosomal DNA functions as mobile enhancers to globally amplify chromosomal transcription. *Cancer Cell* **39**, 694–707.e697 (2021).
- Yi, E. et al. Live-cell imaging shows uneven segregation of extrachromosomal DNA elements and transcriptionally active extrachromosomal DNA hubs in cancer. *Cancer Discov.* **12**, 468–483 (2022).
- Nathanson, D. A. et al. Targeted therapy resistance mediated by dynamic regulation of extrachromosomal mutant EGFR DNA. *Science* **343**, 72–76 (2014).
- Lange, J. T. et al. The evolutionary dynamics of extrachromosomal DNA in human cancers. *Nat. Genet.* **54**, 1527–1533 (2022).
- Wu, S. et al. Circular ecDNA promotes accessible chromatin and high oncogene expression. *Nature* **575**, 699–703 (2019).
- Wu, S., Bafna, V. & Mischel, P. S. Extrachromosomal DNA (ecDNA) in cancer pathogenesis. *Curr. Opin. Genet. Dev.* **66**, 78–82 (2021).
- Morton, A. R. et al. Functional enhancers shape extrachromosomal oncogene amplifications. *Cell* **179**, 1330–1341.e1313 (2019).
- Hung, K. L. et al. ecDNA hubs drive cooperative intermolecular oncogene expression. *Nature* **600**, 731–736 (2021).
- Luebeck, J. et al. Extrachromosomal DNA in the cancerous transformation of Barrett's oesophagus. *Nature* **616**, 798–805 (2023).
- Kuhn, R., Schwenk, F., Aguet, M. & Rajewsky, K. Inducible gene targeting in mice. *Science* **269**, 1427–1429 (1995).
- Abramski, K. & Hoess, R. Bacteriophage P1 site-specific recombination. Purification and properties of the Cre recombinase protein. *J. Biol. Chem.* **259**, 1509–1514 (1984).
- Lengauer, C., Kinzler, K. W. & Vogelstein, B. Genetic instability in colorectal cancers. *Nature* **386**, 623–627 (1997).
- Haupt, Y., Maya, R., Kazaz, A. & Oren, M. Mdm2 promotes the rapid degradation of p53. *Nature* **387**, 296–299 (1997).
- Kubbutat, M. H., Jones, S. N. & Vousden, K. H. Regulation of p53 stability by Mdm2. *Nature* **387**, 299–303 (1997).
- Oliner, J. D., Saiki, A. Y. & Caenepeel, S. The role of MDM2 amplification and overexpression in tumorigenesis. *Cold Spring Harb. Perspect. Med.* **6**, a026336 (2016).
- Jones, S. N., Roe, A. E., Donehower, L. A. & Bradley, A. Rescue of embryonic lethality in Mdm2-deficient mice by absence of p53. *Nature* **378**, 206–208 (1995).
- Montes de Oca Luna, R., Wagner, D. S. & Lozano, G. Rescue of early embryonic lethality in mdm2-deficient mice by deletion of p53. *Nature* **378**, 203–206 (1995).
- Song, K. et al. Plasticity of extrachromosomal and intrachromosomal BRAF amplifications in overcoming targeted therapy dosage challenges. *Cancer Discov.* **12**, 1046–1069 (2022).
- Serrano, M., Lin, A. W., McCurrach, M. E., Beach, D. & Lowe, S. W. Oncogenic ras provokes premature cell senescence associated with accumulation of p53 and p16^{INK4a}. *Cell* **88**, 593–602 (1997).
- Binh, M. B. et al. MDM2 and CDK4 immunostainings are useful adjuncts in diagnosing well-differentiated and dedifferentiated liposarcoma subtypes: a comparative analysis of 559 soft tissue neoplasms with genetic data. *Am. J. Surg. Pathol.* **29**, 1340–1347 (2005).
- Gounder, M. M. et al. A first-in-human phase I study of milademetan, an MDM2 inhibitor, in patients with advanced liposarcoma, solid tumors, or lymphomas. *J. Clin. Oncol.* **41**, 1714–1724 (2023).

32. Lewandoski, M., Meyers, E. N. & Martin, G. R. Analysis of *Fgf8* gene function in vertebrate development. *Cold Spring Harb. Symp. Quant. Biol.* **62**, 159–168 (1997).
33. Moon, H., Park, H. & Ro, S. W. c-Myc-driven hepatocarcinogenesis. *Anticancer Res.* **41**, 4937–4946 (2021).
34. Molina-Sánchez, P. et al. Cooperation between distinct cancer driver genes underlies intertumor heterogeneity in hepatocellular carcinoma. *Gastroenterology* **159**, 2203–2220.e2214 (2020).
35. Moller, H. D. et al. CRISPR-C: circularization of genes and chromosome by CRISPR in human cells. *Nucleic Acids Res.* **46**, e131 (2018).
36. Hoff, Von et al. Hydroxyurea accelerates loss of extrachromosomally amplified genes from tumor cells. *Cancer Res.* **51**, 6273–6279 (1991).
37. Weng, W., Liu, X., Lui, K. O. & Zhou, B. Harnessing orthogonal recombinases to decipher cell fate with enhanced precision. *Trends Cell Biol.* **32**, 324–337 (2022).
38. Penn, L. J., Brooks, M. W., Laufer, E. M. & Land, H. Negative autoregulation of c-myc transcription. *EMBO J.* **9**, 1113–1121 (1990).
39. Grignani, F. et al. Negative autoregulation of c-myc gene expression is inactivated in transformed cells. *EMBO J.* **9**, 3913–3922 (1990).
40. Sivak, L. E. et al. Autoregulation of the human N-myc oncogene is disrupted in amplified but not single-copy neuroblastoma cell lines. *Oncogene* **15**, 1937–1946 (1997).
41. Jones, S. N., Hancock, A. R., Vogel, H., Donehower, L. A. & Bradley, A. Overexpression of Mdm2 in mice reveals a p53-independent role for Mdm2 in tumorigenesis. *Proc. Natl Acad. Sci. USA* **95**, 15608–15612 (1998).
42. Donehower, L. A. et al. Mice deficient for p53 are developmentally normal but susceptible to spontaneous tumours. *Nature* **356**, 215–221 (1992).
43. Jacks, T. et al. Tumor spectrum analysis in p53-mutant mice. *Curr. Biol.* **4**, 1–7 (1994).

Publisher's note Springer Nature remains neutral with regard to jurisdictional claims in published maps and institutional affiliations.



Open Access This article is licensed under a Creative Commons Attribution-NonCommercial-NoDerivatives 4.0 International License, which permits any non-commercial use, sharing, distribution and reproduction in any medium or format, as long as you give appropriate credit to the original author(s) and the source, provide a link to the Creative Commons licence, and indicate if you modified the licensed material. You do not have permission under this licence to share adapted material derived from this article or parts of it. The images or other third party material in this article are included in the article's Creative Commons licence, unless indicated otherwise in a credit line to the material. If material is not included in the article's Creative Commons licence and your intended use is not permitted by statutory regulation or exceeds the permitted use, you will need to obtain permission directly from the copyright holder. To view a copy of this licence, visit <http://creativecommons.org/licenses/by-nc-nd/4.0/>.

© The Author(s) 2024

Methods

Plasmids and viral vectors

Plasmids containing the circularization cassettes were generated using a NEBuilder HiFi DNA Assembly Cloning Kit (New England BioLabs, E5520S) and KLD Enzyme Mix (New England BioLabs, MO554S) and validated by Sanger sequencing. Purified, high-titre recombinant adenoviruses encoding Cre (AdCre) were purchased from ViraQuest (VQ-Ad-CMV-Cre; 1×10^{12} particles per millilitre; catalogue no. 091317) and University of Iowa (Ad5CAGCre; VVC-U of Iowa-8193, University of Iowa). pBABE-Puro and pBABE-Puro-HRAS^{G12V} plasmids were obtained from Addgene. For retrovirus production, HEK-293T cells were seeded in high-glucose Dulbecco's modified Eagle medium (DMEM) supplemented with 10% heat-inactivated fetal bovine serum (FBS) without antibiotics in 100 mm petri dishes. The next day, cells at approximately 60–70% confluence were transfected with 20 µg of retroviral vector carrying the HRAS^{G12V} cDNA or a control vector, 5 µg of packaging plasmid and 1 µg of envelope plasmid. After 24 h, the medium was replaced with DMEM with antibiotics. Cells were incubated for 48 h with two consecutive collections of the medium containing the retroviral particles at 24 and 48 h. Medium collected at 24 and 48 h was filtered using a 0.45 µm filter unit and used to transduce MEF cells. Retroviral infection was performed, incubating cells with viral supernatant supplemented with polybrene (0.2 µl ml⁻¹; Millipore Sigma, TR-1003G).

Cell culture

The culture medium for HCT116 cells (ATCC, CCL-247) was McCoy's 5A Medium Modified (Thermo Fisher Scientific, catalogue no. 16600108) supplemented with 10% heat-inactivated FBS (Sigma-Aldrich, F2442), penicillin-streptomycin (100 U l⁻¹; Gemini Bio-Products, catalogue no. 400-109). For selection of targeted cells engineered with the circularization cassettes, the following antibiotics were used: puromycin (2 µg ml⁻¹; Sigma-Aldrich, P9620), hygromycin B (200 µg ml⁻¹; Thermo Fisher Scientific, catalogue no. 10687010). HEK-293T cells for viral vector production were cultured in high-glucose DMEM (4.5 g l⁻¹; Thermo Fisher Scientific, catalogue no. 11995065) with 10% heat-inactivated FBS, L-glutamine (2 mM), and penicillin-streptomycin (100 U l⁻¹).

MEFs with different genotypes were isolated from E13.5 mouse embryos and propagated in high-glucose DMEM supplemented with 10% heat-inactivated FBS, L-glutamine (2 mM) and penicillin-streptomycin (100 U l⁻¹).

aNSCs were isolated and cultured following the protocol described by Ahmed et al.⁴⁴. Upon isolation, aNSC were maintained as neurospheres and then allowed to attach to laminin-coated (Sigma-Aldrich, L2020) dishes in NeuroCult Stem Cell Basal Media with NeuroCult Proliferation Supplement (Mouse & Rat) (Stem Cells Technologies, catalogue no. 05702), 20 ng ml⁻¹EGF (Stem Cells Technologies, catalogue no. 78006), 10 ng ml⁻¹bFGF (Stem Cells Technologies, catalogue no. 78003), and 2 µg ml⁻¹heparin (Stem Cell Technologies, 07980).

Cerebellar stem cells were isolated from the cerebella of 5-day-old mice. Cerebella were digested using a Papain Dissociation system (Worthington, LK003150) to obtain a single-cell suspension. Cells were washed and suspended in flow buffer (phosphate-buffered saline (PBS) supplemented with 2% heat-inactivated FBS (Sigma-Aldrich, F2442), 2 mM EDTA and 25 mM HEPES (Thermo Scientific, catalogue no. 15630080)) and passed through a 40 µm cell strainer. Cells were stained for prominin-1 and lineage markers and sorted. Cerebellar stem cells (prominin-1-positive, lineage-negative) were allowed to attach to laminin-coated (Sigma-Aldrich, L2020) dishes in NeuroCult Stem Cell Basal Media with NeuroCult Proliferation Supplement (Mouse & Rat) (Stem Cells Technologies, catalogue no. 05702), 20 ng ml⁻¹EGF (Stem Cells Technologies, catalogue no. 78006), 10 ng ml⁻¹bFGF (Stem Cells Technologies, catalogue no. 78003) and 2 µg ml⁻¹heparin (Stem Cell Technologies, catalogue no. 07980).

Primary hepatocytes were isolated from the livers of adult mice. Following euthanasia, the liver was rapidly perfused with PBS, chopped into small pieces and digested in 3.42 mg ml⁻¹ dispase II (Roche, catalogue no. 04942078001) and 1 mg ml⁻¹collagenase IV (Sigma-Aldrich, C5138) in DMEM. The hepatocyte fraction was isolated by centrifugation at 200g and plated on collagen-coated plates. Culture media for hepatocytes consisted of William's E media (Gibco, A1217601) with supplements: 10% heat-inactivated FBS (Sigma-Aldrich, F2442), 10 mM nicotinamide, 2 mM glutamine, 0.1 mM dexamethasone, 1×ITS+ (Gibco, catalogue no. 41-400-045), 0.2 mMascorbic acid, 20 mM HEPES (Thermo Scientific, catalogue no. 15630080), 1 mM sodium pyruvate, 14 mMglucose (Gibco, A2494001), penicillin-streptomycin (100 U l⁻¹). Hepatocytes were subsequently immortalized by infection with Ad-Tbg-Cre (Addgene, 107787-AAV8).

All cells were negative for mycoplasma contamination. Cells were maintained in a humidified, 5% CO₂ atmosphere at 37 °C.

In vivo tumorigenesis

For in vivo tumour formation assays, nude mice were injected in the flank with 400,000–1,000,000 pBABE-Puro-HRASG12V transduced MEFs of the indicated genotype. Mice were monitored every 2–3 days and euthanized when the tumour volume reached 2 cc.

ATAC-seq analysis

ATAC-seq libraries were generated and sequenced by the Memorial Sloan Kettering Cancer Center (MSKCC) genomic core. Fastq files from ATAC-seq and WGS were aligned to the mouse genome (mm10) using Bowtie2. Then, CNVkit (v.0.9.10) was applied to WGS bam files to identify copy number variations and ecDNA amplicon regions. To compare ATAC-seq signals between ecDNA amplicons and corresponding chromosomal regions, bamCoverage in deeptools (v.3.5.3) was used to calculate read counts with 10 kb bin size, and MACS (v.3.0.0b1) was used for peak calling. Read counts and peak numbers were normalized by segment length (10 kb), sequencing depth and copy number.

Homologous recombination in HCT116 cells

HCT116 cells were obtained directly from ATCC (ATCC, CCL-247). Cas9 protein, CRISPR RNA (crRNA) and *trans*-activating crRNA (tracrRNA) were purchased from Integrated DNA Technologies and preassembled by incubation according to the manufacturer's instructions.

The two circularization cassettes were introduced sequentially. The donor cassettes were amplified using primers containing an 80 nucleotide 5' homology sequence to the desired targeting site. Then, 100–500 ng of gel-purified PCR products were transfected into 500,000 HCT116 cells plated the day before in a well of a six-well plate using Lipofectamine 3000 (Thermo Fisher, L3000008). Two hours later, the preassembled Cas9-crRNA-tracrRNA were introduced using Lipofectamine CRISPR-Max (Thermo Fisher, CMAX00008) following the manufacturer's instructions. Selection with either puromycin (5' cassette, 2 µg ml⁻¹) or hygromycin (3' cassette, 200 µg ml⁻¹) was started 48 h after transfection. Surviving clones were isolated and screened by PCR, followed by Sanger sequencing to detect correct targeting.

Animals

All animal experiments were approved by the Institutional Animal Care and Use Committee of MSKCC. To generate the *Myc*^{ec} (JAX strain: 039221) and *Mdm2*^{ec} (JAX strain: 039222) mouse strains in a C57BL/6J background, zygote electroporation based on published protocols⁴⁵ was carried out by the MSKCC Mouse Genetics Core Facility using crRNAs experimentally validated in mouse embryonic stem cells. Briefly, multiple zygotes placed in an electrode chamber were subjected to electroporation at one time. Each electroporation mixture contained the 5'(AGATGCCACAGAAAGTGG) and 3'(ATCATGAGTTGAGTTCACTC) breakpoint targeting crRNAs (25 ng µl⁻¹), S.p. Cas9 V3 protein (100 ng µl⁻¹; IDT), and two single-stranded oligodeoxynucleotides

Article

of 159 bp with asymmetric homology arms (200 ng μl^{-1}) in a solution of 0.1% polyvinyl alcohol. Electroporated zygotes were cultured in KSOM medium at 37 °C and 5% CO₂ until the two-cell stage; after that, they were transferred to the oviducts of pseudopregnant females on the day of the vaginal plug. N₀ animals generated from the zygotes were genotyped and Sanger sequenced to confirm insertion of both *loxP*sites. Double-targeted N₀ mice were mated to C57BL/6J wild-type mice to generate *Myc*^{ec/+} F₁ progeny. Primers for genotyping are listed in Supplementary Table 4. The *Mdm2*^{ec} mouse was also generated as described above, except that guide RNAs were used to target chr. 10: 116711442 (TCTTACAGCATACTACGGTC TGG) and chr. 10: 118002454 (TTCTGCGATTCTGTATCGCT AGG) for the 5' and 3' *loxP* insertion sites, respectively.

Liver tumours were generated by hydrodynamic tail-vein injection of a solution of sterile saline containing 25 μg of pT3-EF1a-MYC-IRES-Luc and 5 μg of transposase-encoding vector (SB13). In brief, a volume equivalent to 10% of the mouse's body weight was injected through the tail vein using a 3 ml syringe with 26-gauge \times 5/8-inch needle. A mix of male and female mice were used for these experiments. Mice were monitored for tumour development and euthanized at the humane end point. The *CMV-SB13* and *pT3-loxP-EF1a-MYC-IRES-Luc-loxP* were gifts from A. Lujambio (Icahn School of Medicine at Mount Sinai). *pT3-EF1a-MYC-IRES-Luc* was generated by removing the *loxP*sites from *pT3-loxP-EF1a-MYC-IRES-Luc-loxP*. *p53*^{f/f} (B6.129P2-Trp53tm1Brn/J) (strain: 008462)⁴⁶, *Actin-Cre* (B6N.FVB-Tmem163Tg(ACTB-Cre)2Mrt/CjDswJ (strain: 019099)³², *Vil1-Cre* (B6.Cg-Tg(Vil1-cre)1000Gum/J; strain: 021504)⁴⁷, *Atoh1-Cre* (B6.Cg-Tg(Atoh1-cre)1Bfri/J; strain: 011104)⁴⁸, *Alb-Cre* (B6.Cg-Speer6-ps1Tg(Alb-cre)21Mgn/J; strain: 003574)⁴⁹, *Mx-Cre* (B6.Cg-Tg(Mx1-cre)1Cgn/J; strain: 003556)²⁰ and *Nestin-Cre* (B6.Cg-Tg(Nes-cre)1Kln/J)^{50,51} mouse strains were obtained from the Jackson Laboratory. Outbred athymic nude mice (stock: 007850) were purchased from the Jackson Laboratory.

Antibodies and immunoblots

Cells were lysed in Laemml buffer, supplemented with protease (cComplete; Roche, COEDTAF-RO) and phosphatase (EDTA-free Protease Inhibitor Cocktail; Roche, PHOSS-RO) inhibitors. Proteins were separated by sodium dodecyl sulfate polyacrylamide gel electrophoresis and analysed by western blotting using standard procedures. After protein transfer, the nitrocellulose membranes (Bio-Rad, catalogue no. 1704271) were blocked by incubation with LICOR Intercept (TBS) blocking buffer. The following primary antibodies were used: anti-vinculin (1:5,000; Millipore, MAB3574), anti-c-MYC (1:1,000; Cell Signaling, D84C12), anti-MDM2 (1:1,000; Cell Signaling, 51541), anti- α -tubulin (1:5,000; Cell Signaling, 3873), anti-p53 (1:1,000; Leica Biosystems, P53-PROTEIN-CMS) and anti-p21 (1:1,000; Cell Signaling, 64016). The following secondary antibodies were used: IRDye 800 anti-rabbit (LICOR, 926-32213) and IRDye 680 anti-mouse (LICOR, 926-68072). Images were acquired using an Odyssey Imaging System (LICOR).

Flow cytometry and cell sorting

Flow cytometry analysis of ecMDM2 and invMDM2 HCT116 cells was performed following collection of cells in a single-cell suspension. Cells were resuspended in flow buffer (PBS supplemented with 2% heat-inactivated FBS (Sigma-Aldrich, F2442), 2 mM EDTA, and 25 mM HEPES (Thermo Scientific, catalogue no. 15630080)) and passed through a 40 μm cell strainer to remove clumps. DAPI (Thermo Scientific, D1306) staining was used to discriminate between live and dead cells. Flow cytometry analyses were performed on LSR Fortessa (BD Biosciences) instruments. Cells were first gated on the basis of size (forward scatter, FSC) and density and/or granularity (side scatter, SSC), excluding debris and doublets; DAPI staining was used to gate the live fraction. Then, polygonal or quadrant gates were applied to isolate the population of interest on the basis of GFP and mScarlet expression. The same protocol was used to sort ecMDM2 and invMDM2 HCT116

double-positive cells using FACSAria (BD Biosciences) and FACSsymphony (BD Biosciences) instruments.

For isolation of cerebellar stem cells, cells were incubated for 1 h with Cd133 (prominin-1) monoclonal antibody (13A4)-FITC (1:100; Thermo Scientific 311-1331-80), Cd81 monoclonal antibody (Eat2)-PE (1:50; Thermo Scientific, MA517941), anti-O4-PE (1:50; Miltenyi Biotec., 130-117-507) and anti-PSA-NCAM-PE (Miltenyi Biotec. 130-117-394, 1:50). After staining, cells were washed and sorted using a BD FACSAria III instrument (BD Biosciences) according to prominin-1-positive and lineage-negative (Cd81⁺; O4⁺; PSA/NCAM⁺) marker expression. The gating strategy is provided in Supplementary Fig. 1, which contains the uncropped gel images.

Tissue processing and immunohistochemistry

Subcutaneous tumours and livers were fixed for 24 h in 10% formalin and then transferred to 70% ethanol for at least 24 h before paraffin embedding and sectioning. Unstained 5 μm tissue sections were deparaffinized in Histo-Clear II (Electron Microscopy Sciences, catalogue no. 64110-04) and rehydrated with graded alcohols to distilled water. Endogenous peroxidase activity was inactivated using 3% H₂O₂ (MP Biomedicals, catalogue no. 194057) for 15 min. Tissue slides were pre-treated for antigen retrieval by heating in Antigen Unmasking Solution, Citrate-Based (Vector Laboratories H-3300) using a pressure cooker. Non-specific protein interactions were blocked in 10% normal serum for 30 min. Slides were incubated in primary antibody overnight at 4 °C at the following dilutions: HNF4 α (1:500; CST, 3113T); CK19 (1:500; Abcam, AB52625). VectaStain ABC-HRP Rabbit IgG (Vector Laboratories, PK-6101) was used as the secondary antibody, with incubation according to the manufacturer's instructions. ImmPACT DAB (Vector Laboratories SK-4105) was used as a substrate. Haematoxylin (Vector Laboratories, H-3401) was used as the counterstain. Cover slides were mounted with VectaMount Express Mounting Medium (Vector Laboratories, H-5700). Bright-field images were obtained using a Zeiss AxioCam microscope. Haematoxylin and eosin slides were examined by C.A. and C.S., board-certified pathologists with extensive expertise in human sarcomas and liposarcomas (C.A.) and human liver cancers (C.S.).

RNA extraction and qPCR with reverse transcription

Total RNA was isolated using an RNeasy Mini Kit (QIAGEN, catalogue no. 74106) according to the manufacturer's instructions. After treatment with DNase I (Ambion, AM2222), 1 μg of purified RNA was retrotranscribed with oligos d(T)₁₈ using a SuperScript IV First-strand System (Invitrogen, catalogue no. 18091050). For qPCR with reverse transcription (RT-qPCR), an aliquot of the RT reaction was analysed with PowerUp SYBR Green (Applied Biosystems, A25777) and a QuantStudio 6 Flex real-time PCR system (Applied Biosystems). Target transcript levels were normalized to those of the indicated reference genes. The expression of each gene was measured in at least three independent experiments.

Milademetan dose-response curve

A total of 1,500 cells were seeded in each well of a 96-well plate, with 100 μl of complete medium per well. Cells were allowed to adhere for 12 h in the incubator before the treatment was initiated. Milademetan (MedChemExpress, HY-101266) doses ranging from 20 to 10,240 nM were prepared, along with a vehicle control at the highest treatment dose. The doses were added to the respective wells in a volume of 100 μl , ensuring that the cells received milademetan doses ranging from 10 to 5,120 nM. After a 72 h incubation period, cell viability was determined using the Cell-TiterGlo assay (Promega, G7570), following manufacturer's instructions. Briefly, the assay reagent was added to the wells, and the plates were gently agitated to ensure thorough mixing. The luminescence signal was then measured using a Synergy 2 plate reader (Biotek) according to the manufacturer's guidelines.

Gene copy number assay

Myc, *MDM2* and *Mdm2* gene amplification was evaluated using TaqMan Copy Number Assays (probe Mm00734221_cn, probe Hs02873318_cn and probe Mm00312030_cn) using the QuantStudio 6 Flex real-time PCR system. Briefly, genomic DNA was amplified using the TaqPath ProAmp Master Mix (Applied Biosystems, A30865) kit and following the supplier's instructions. TaqMan Copy Number Reference Assay (Tfrc, 4458367 and TERT, 4403316) were used in duplex as references for mouse and human genomes, respectively. Relative copy number variations were calculated using the ddCt method.

Digital droplet PCR

Assays specific for the detection of Cre-mediated circularization and excision of the mouse *Myc*^{ec} or *Mdm2*^{ec} allele were designed and ordered through Bio-Rad (Supplementary Table 4). Cycling conditions were tested to ensure optimal annealing and extension temperatures, as well as optimal separation of positive and empty droplets. Optimization was done with a known positive control. After PicoGreen quantification, 0.4–9.0 ng genomic DNA was combined with locus-specific primers, FAM- and HEX-labelled probes, BamHI and digital PCR Supermix for probes (no dUTP). All reactions were performed on a QX200 digital droplet PCR system (Bio-Rad, catalogue no.:1864001), and each sample was evaluated in technical duplicates using *Ptger2* as a reference. Reactions were partitioned into a mean of approximately 21,000 droplets per well using a QX200 droplet generator. Emulsified PCRs were run on a 96-well thermal cycler, using cycling conditions identified during the optimization step (95 °C 10 min; 40 cycles of 94 °C 30 s and 56 °C 1 min; 98 °C 10 min; 4 °C hold). Plates were read and analysed with QuantaSoft software (Bio-Rad; v.1.7) to assess the number of droplets positive for the gene of interest, reference gene, both or neither.

RNA-seq and gene set enrichment analysis

Paired-end RNA libraries were sequenced by the MSKCC integrated genomics core. Reads were mapped to mm10 using the STAR aligner⁵², and differential gene expression was calculated using the DESeq2 R package⁵³. For gene set enrichment analysis, genes were ranked on the basis of their moderated *P* value [$-\log_{10}(\text{adjusted } P) \times \text{sign}(\log_2(\text{fold change}))$], and gene sets were obtained from the HALLMARK msigdb pathways database. Enrichment was calculated using the fgsea R package.

Shallow whole-genome sequencing

The sWGS was carried out by the Integrated Genomics Operation core at MSKCC. Briefly, after PicoGreen quantification and quality control by Agilent BioAnalyzer, 100 ng of genomic DNA was sheared using a LE220-plus Focused-ultrasonicator (Covaris, catalogue no. 500560), and sequencing libraries were prepared using a KAPA Hyper Prep Kit (Kapa Biosystems, KK8504) with eight cycles of PCR. Samples were run on a NovaSeq 6000 in a PE100 run, using a NovaSeq 6000 S4 Reagent Kit v.1.5 (200 cycles) (Illumina). Paired-end genomic DNA libraries were sequenced by the MSKCC integrated genomics core. Reads were mapped to mm10 or hg19 using the Bowtie2 aligner⁵⁴. To calculate genome coverage and copy number changes, we used the QDNAseq R package⁵⁵ with 15 kb bins. Plots were generated using the Gviz package⁵⁶.

Amplicon Architect analysis

We used the AmpliconSuite-pipeline (v.0.1555.1, <https://github.com/AmpliconSuite/AmpliconSuite-pipeline>) to invoke AmpliconArchitect⁵⁷ (v.1.3.r5) on a collection of copy-number seed regions generated using CNVkit⁵⁸ (v.0.9.9), with default settings.

Metaphase chromosome spread analysis

Cells were incubated with KaryoMAX (catalogue no. 15212012; Thermo Fisher Scientific) treatment at 0.05 µg ml⁻¹ for 1 h (mouse cells) or at

0.1 µg ml⁻¹ for 1 h and 30 min (human cells). A single-cell suspension was then collected, washed in PBS, and treated with 75 mM KCl for 10 min at 37 °C. Samples were then fixed in ice-cold 3:1 methanol/glacial acetic acid (Carnoy's fixative) for 20 min and washed a further three times with Carnoy's fixative. Fixed cells were dropped onto a glass slide in a humidified chamber and counterstained with DAPI (Vector Laboratories, H-1800). Images were acquired with an AX10 Imager.Z1 Zeiss microscope through a ×63 objective lens. Zeiss Zen 2.3 Pro software was used for image acquisition. Fiji (v.2.0.0-rc-65/1.15w) was used for image analysis and for brightness and contrast adjustments. Fiji's 'Invert LUT' and 'Shadows' postprocessing commands were sequentially applied to better visualize ecDNAs.

FISH analysis

DNA FISH was performed on fixed cells using a two-colour probe. *MDM2* (green dUTP) and centromeric control (orange dUTP) FISH probes were purchased from Empire Genomics (SKU MDM2-CHR12). BAC clones containing the murine *Myc* locus (RP23-130M7, RP23-342F3 RP23-454G15) were labelled with red dUTP, and RP23-333G9 (15qA1) labelled with green dUTP served as the control. *Myc* (RP23-307D14-ORANGE) and centromeric control (RP23-333G9-GREEN) FISH probes were also purchased from Empire Genomics. All RP23 clones were purchased from the Roswell Park Cancer Institute Genomics Shared Resource.

Probe labelling, hybridization, posthybridization washing and fluorescence detection were performed according to procedures established at the Molecular Cytogenetics Core Facility. Slides were scanned using a Zeiss AxioPlan 2i epifluorescence microscope (Carl Zeiss Microscopy) equipped with Isis imaging software (MetaSystems Group Inc.) or Leica SP5 confocal microscope (Leica) with a ×63 objective. The entire hybridized area was scanned through a ×63 objective lens to assess the quality of hybridization and signal pattern. To the extent possible, apoptotic cells and bodies were excluded.

The BAC clone RP23-428D5 (BACPAC) was used for detection of the murine *Mdm2* locus, and the BAC clone RP23-309H16 was used for the detection of murine 10qA1 (Cen10). Following inoculation, bacterial cells were pelleted, and BAC DNA was extracted using a NucleoBond Xtra BAC kit (Takara, catalogue no. 740436) as per the manufacturer's instructions. The probe for *Mdm2* was labelled with ChromaTide Alexa Fluor 568-5-dUTP (Thermo, C11399), and the Cen10 probe was labelled with ChromaTide Alexa Fluor 488-5-dUTP (Thermo, C11397) as per manufacturer's instructions. Before hybridization, the labelled probe was preannealed with mouse COT-1 DNA in hybridization buffer (2×SSC, 50% formamide, 10% dextran sulfate) for 90 min at 37 °C. Hybridization of slides using preannealed probes was performed at 72 °C for 2 min, followed by 37 °C overnight. Posthybridization washes were conducted in 0.4×SSC/0.3% Igepal at 72 °C for 2 min, followed by 2×SSC at room temperature for 5 min. Slides were then rinsed briefly in water, air-dried, counterstained with DAPI (Thermo, D1306) and mounted with Prolong Diamond Antifade Mountant (Thermo, P36965). Images were acquired in the MSKCC Molecular Cytology Core using a Zeiss Imager equipped with a Zeiss AxioCam Mrm camera and a ×100 oil objective. Specimens for DNA FISH were embedded in optimal cutting temperature compound and stored at -80 °C before analysis.

RNA in situ hybridization

Mdm2 RNA FISH was performed in collaboration with the MSKCC Molecular Cytology Core. Briefly, paraffin-embedded tissue sections were cut at 5 µm and kept at 4 °C. Samples were loaded into a Leica Bond RX autostainer, baked for 30 min at 60 °C, dewaxed with Bond Dewax Solution (Leica, AR9222) and pretreated with EDTA-based epitope retrieval ER2 solution (Leica, AR9640) for 15 min at 95 °C. The mouse *Mdm2* probe (Advanced Cell Diagnostics (ACD), catalogue no. 447648) was hybridized for 2 h at 42 °C. Mouse PPIB (ACD, catalogue no. 313918) and dapB (ACD, catalogue no. 312038) probes were used as positive and

Article

negative controls, respectively. The hybridized probes were detected using an RNAscope 2.5 LS Reagent Kit – Brown (ACD, catalogue no. 322100) according to the manufacturer's instructions with the following modifications: DAB application was omitted and replaced with fluorescent CF594/tyramide (Biotium, B40953) for 20 min at room temperature. Images were acquired using a Zeiss Imager equipped with a Zeiss AxioCam Mrm camera, a $\times 20$ air objective and a $\times 100$ oil objective.

Statistics and reproducibility

Paired or unpaired Student's two-tailed *t*-test and one-way ANOVA (corrected for multiple comparisons, Tukey test), were used to compare two or more groups, respectively, and to determine statistical significance (GraphPad Prism 9 and R software). Welch's correction was used for populations with unequal variances. Unless otherwise indicated, the mean value and the standard deviation of each condition are shown. Differences were considered significant at $P < 0.05$.

Materials availability

Materials are available from the corresponding authors upon request. Plasmids containing the 'circularization cassettes' described in this paper are available through Addgene (Plasmids #219563, #219564, #219565). *Myc^{ec}* (strain: 039221) and *Mdm2^{ec}* (strain: 039222) are available through the JAX repository (<https://www.jax.org/>).

Reporting summary

Further information on research design is available in the Nature Portfolio Reporting Summary linked to this article.

Data availability

All datasets have been deposited and made publicly available: sWGS data (GSE264005), bulk RNA-seq data (GSE264003) and ATAC-seq data (GSE264240). AmpliconArchitect outputs for murine *Mdm2*-containing ecDNA (<https://ampliconrepository.org/project/649b3c097dc54138a9d391b3>) and murine *Myc*-containing ecDNA (<https://ampliconrepository.org/project/64839f137dc54138a9d39122>) are available through the AmpliconRepository online repository (<https://ampliconrepository.org/>). Materials are available from the corresponding authors upon request.

44. Ahmed, A., Isaksen, T. J. & Yamashita, T. Protocol for mouse adult neural stem cell isolation and culture. *STAR Protoc.* **2**, 100522 (2021).
45. Hashimoto, M., Yamashita, Y. & Takemoto, T. Electroporation of Cas9 protein/sgRNA into early pronuclear zygotes generates non-mosaic mutants in the mouse. *Dev. Biol.* **418**, 1–9 (2016).
46. Marino, S., Vooijs, M., van Der Gulden, H., Jonkers, J. & Berns, A. Induction of medulloblastomas in p53-null mutant mice by somatic inactivation of *Rb* in the external granular layer cells of the cerebellum. *Genes Dev.* **14**, 994–1004 (2000).
47. Madison, B. B. et al. Cis elements of the villin gene control expression in restricted domains of the vertical (crypt) and horizontal (duodenum, cecum) axes of the intestine. *J. Biol. Chem.* **277**, 33275–33283 (2002).
48. Matei, V. et al. Smaller inner ear sensory epithelia in Neurog1 null mice are related to earlier hair cell cycle exit. *Dev. Dyn.* **234**, 633–650 (2005).
49. Postic, C. et al. Dual roles for glucokinase in glucose homeostasis as determined by liver and pancreatic β cell-specific gene knock-outs using Cre recombinase. *J. Biol. Chem.* **274**, 303–315 (1999).
50. Giusti, S. A. et al. Behavioral phenotyping of Nestin-Cre mice: implications for genetic mouse models of psychiatric disorders. *J. Psychiatr. Res.* **55**, 87–95 (2014).

51. Tronche, F. et al. Disruption of the glucocorticoid receptor gene in the nervous system results in reduced anxiety. *Nat. Genet.* **23**, 99–103 (1999).
52. Dobin, A. et al. STAR: ultrafast universal RNA-seq aligner. *Bioinformatics* **29**, 15–21 (2013).
53. Love, M. I., Huber, W. & Anders, S. Moderated estimation of fold change and dispersion for RNA-seq data with DESeq2. *Genome Biol.* **15**, 550 (2014).
54. Langmead, B. & Salzberg, S. L. Fast gapped-read alignment with Bowtie 2. *Nat. Methods* **9**, 357–359 (2012).
55. Scheinin, I. et al. DNA copy number analysis of fresh and formalin-fixed specimens by shallow whole-genome sequencing with identification and exclusion of problematic regions in the genome assembly. *Genome Res.* **24**, 2022–2032 (2014).
56. Hahne, F. & Ivanek, R. Visualizing genomic data using Gviz and Bioconductor. *Methods Mol. Biol.* **1418**, 335–351 (2016).
57. Deshpande, V. et al. Exploring the landscape of focal amplifications in cancer using AmpliconArchitect. *Nat. Commun.* **10**, 392 (2019).
58. Talevich, E., Shain, A. H., Botton, T. & Bastian, B. C. CNVkit: genome-wide copy number detection and visualization from targeted DNA sequencing. *PLoS Comput. Biol.* **12**, e1004873 (2016).
59. Gorkin, D. U. et al. An atlas of dynamic chromatin landscapes in mouse fetal development. *Nature* **583**, 744–751 (2020).

Acknowledgements We thank the group of G. Lozano for sharing the *Mdm2^{+/+}/p53^{−/−}* double-knockout MEFs used to validate antibodies for western blotting. This work was supported by grants from NIH-NCI (P30 CA008748 to the MSK Cancer Center, and R01 CA282913 to A.V.), the American Cancer Society Discovery Boost grant (A.V.), the Mark Foundation for Cancer Research ASPIRE grant (A.V.) and a rapid response grant from the Functional Genomics Initiative (A.V.). The research was also supported in part by grants U24CA264379 and R01GM114362 to B.V. D.P. was supported by an AIRC fellowship for Abroad, M.Z. is a recipient of the Paul Calabresi Career Development Award for Clinical Oncology from the Memorial Sloan Kettering K12 Clinical Translational Cancer Research Training Program, M.W. is supported by the Erwin Schrodinger Fellowship from the Austrian Science Fund (FWF, J4723), and M.A.Y. is supported by the Harold E. Varmus Fellowship in Cancer Biology and the Marie-Josée Kravis Women in Science Endeavor (WiSE) fellowship. K.M.G. was supported by an ETIUDA scholarship (no. 2018/28/T/NZ5/00467) funded by the National Science Center, Poland. This work was delivered as part of the eDyNAmiC team supported by the Cancer Grand Challenges partnership funded by Cancer Research UK (CGCATF-2021/100012 and CGCATF-2021/100025) and the National Cancer Institute (OT2CA278688 and OT2CA278635) (H.Y.C., P.S.M., V.B. and A.V.). We thank members of the Cancer Research Emphasis Think Tank, G. Lozano, T. Kelly, B. Stillman, P. Jallepalli, D. Remus and members of the Ben Ezra, Joyner and Lowe laboratories for helpful discussion and advice. Figures 7a, 10a and 12a of the first response in the Peer Review reports were created using BioRender. We thank A. Drilon and M. Repetto for sharing unpublished data on ecDNA in human cancers.

Author contributions A.V. conceived the project and designed the general strategy to generate ecDNAs in vitro and in vivo. R.G., M.A.Y., F.G. and A.V. generated and tested the circularization cassettes; K.M.G., T.M., D.P., M.L., M.A.Y. and A.V. generated and characterized the HCT116 invMDM2 and ecMDM2 cell lines. R.G. generated the *Myc^{ec}* mouse; D.P. characterized the *Myc^{ec}* mouse and performed the experiments in aNSCs, with assistance from H.M.H.N., A.A.Z. and M.L.; M.Z. generated the *Mdm2^{+/+}* mouse and, together with A.V., M.A.Y. and M.W., characterized it and studied the effects of ecDNA formation in MEFs. M.A.Y. and M.Z. generated and characterized the liver cancer model. D.P. and M.Z. generated the RNA-seq data and, together with A.V., analysed them. A.V. analysed the sWGS datasets; Y.C.F. tested the effects of milademetan on *Mdm2^{+/+/-}*-transformed MEFs and performed the PCR with reverse transcription; and G.L.R. and Z.J. performed the western blots. C.R.A. analysed the tumours generated from *Mdm2^{+/+/-}* cells; J.L., B.D. and V.B. performed the Amplicon Architect analysis, Y.P., Z.Z., S.Z., P.S.M., E.G.S. and H.Y.C. analysed the chromatin accessibility datasets. C.M., K.C. and M.O. genotyped and maintained the mouse strains. C.R.A. and C.S. analysed the histology of sarcomas and liver cancers, respectively. D.P., M.Z. and A.V. wrote the manuscript with assistance and comments from all coauthors.

Competing interests H.Y.C. is a cofounder of Accent Therapeutics, Boundless Bio, Cartography Biosciences and Orbital Therapeutics and an advisor for 10x Genomics, Arsenal Biosciences, Chroma Medicine, Exai Bio and Spring Discovery. P.S.M. is a cofounder of, chairs the scientific advisory board of and has equity interest in Boundless Bio. V.B. is a cofounder of, consultant for and SAB member of and has equity interest in Boundless Bio, Inc. and Abterra, Inc. The remaining authors declare no competing interests.

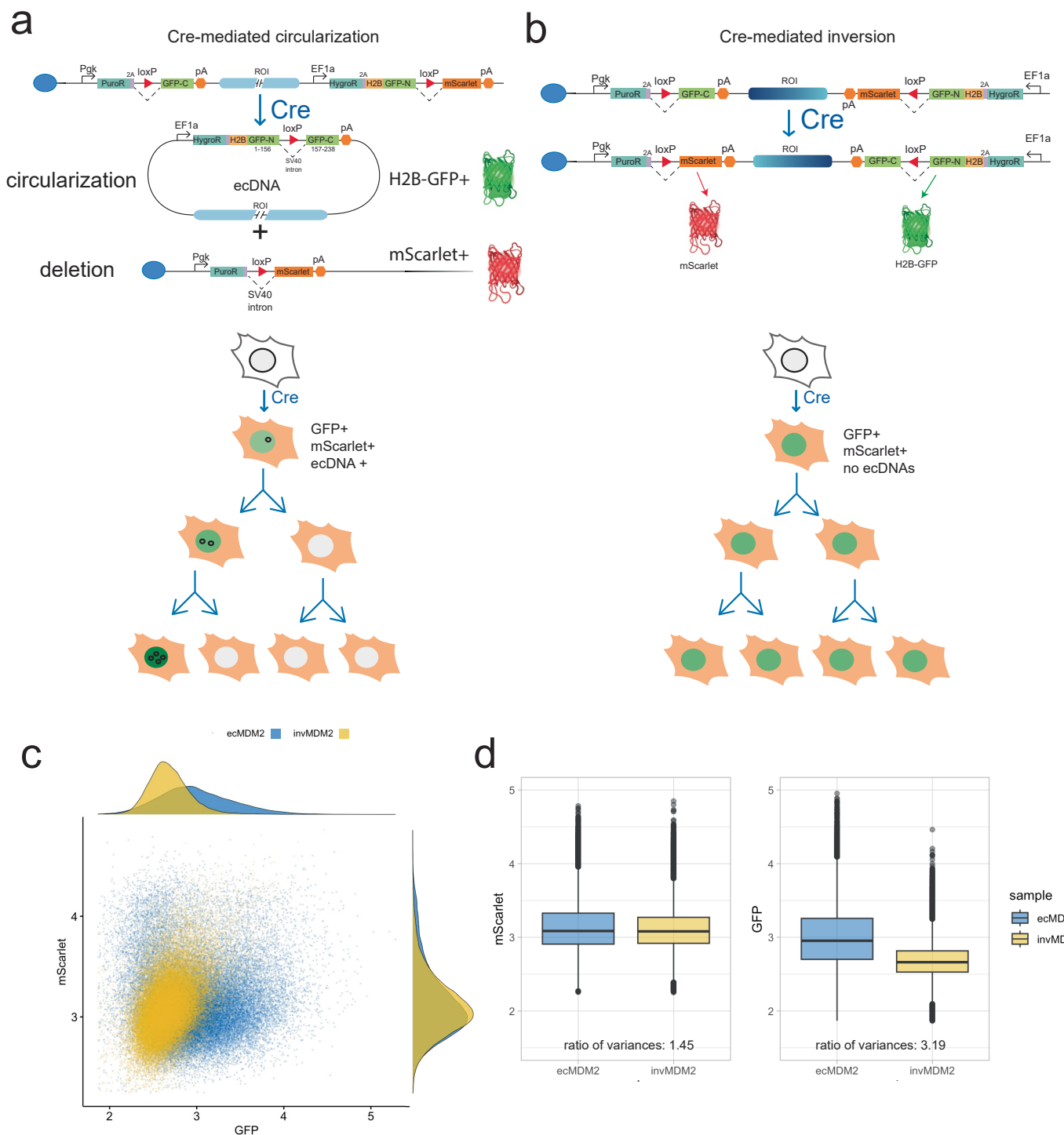
Additional information

Supplementary information The online version contains supplementary material available at <https://doi.org/10.1038/s41586-024-08318-8>.

Correspondence and requests for materials should be addressed to Andrea Ventura.

Peer review information *Nature* thanks Eric Holland and the other, anonymous, reviewer(s) for their contribution to the peer review of this work. Peer reviewer reports are available.

Reprints and permissions information is available at <http://www.nature.com/reprints>.



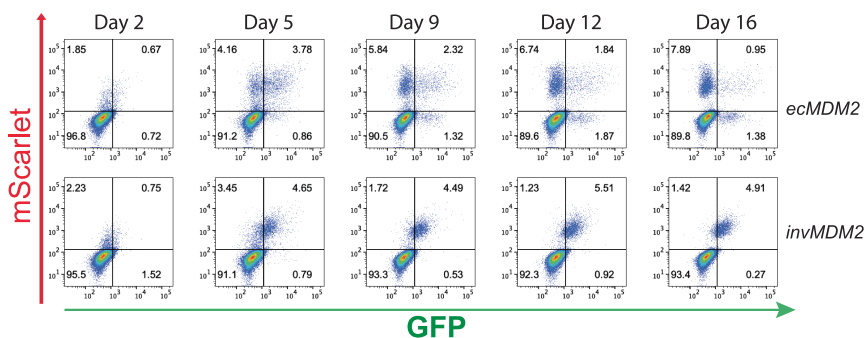
Extended Data Fig. 1 | Generation of ecMDM2 and invMDM2 cells.

a. Schematic and predicted outcomes of the circularization strategy. Upon Cre-mediated recombination, ecDNAs encoding GFP are generated, while mScarlet is expressed from the linear chromosome harboring the corresponding deletion. Random segregation of the ecDNAs will lead some cells to acquire extra copies of the ecDNAs and therefore become more strongly positive for GFP, while other cells will lose the ecDNAs and become GFP-negative. **b.** Schematic and predicted outcome of the inversion strategy. In this allele, the 3' circularization cassette is inserted at the same location as in the ecDNA allele, but with opposite orientation. Upon Cre-mediated recombination, the entire region is inverted resulting in the expression of both GFP and mScarlet reporters. Because both reporters remain on the

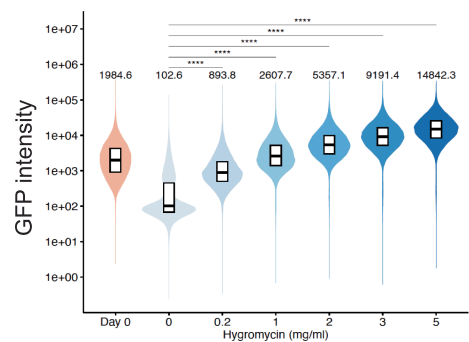
chromosome, the resulting cells are predicted to remain double positive for mScarlet and GFP indefinitely. **c.** ecMDM2 and invMDM2 cells were infected with AdCre, and then sorted for GFP+;mScarlet+ population. The mScarlet vs. GFP scatter plots of post-sorted double positive cells are overlaid, and the density plots for each fluorescence are shown on their respective axes. **d.** Box-and-whiskers plots comparing mScarlet or GFP fluorescence of sorted double positive ecMDM2 and invMDM2 cells, respectively, with indicated ratio of variances as determined by the F-test. $n = 43760$ cell for ecMDM2 and 48911 cells for invMDM2. Boxplot represents upper quartile, median, lower quartile. Whiskers extend to $\pm 1.5 \times$ IQR. Illustrations in **a** and **b** were created using BioRender (<https://biorender.com>).

Article

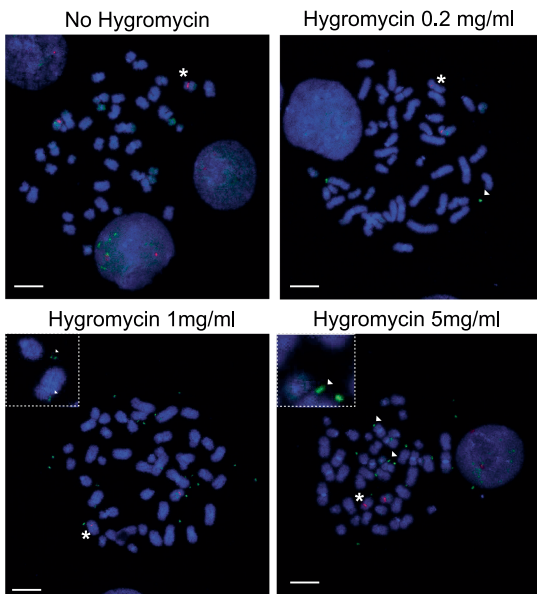
a



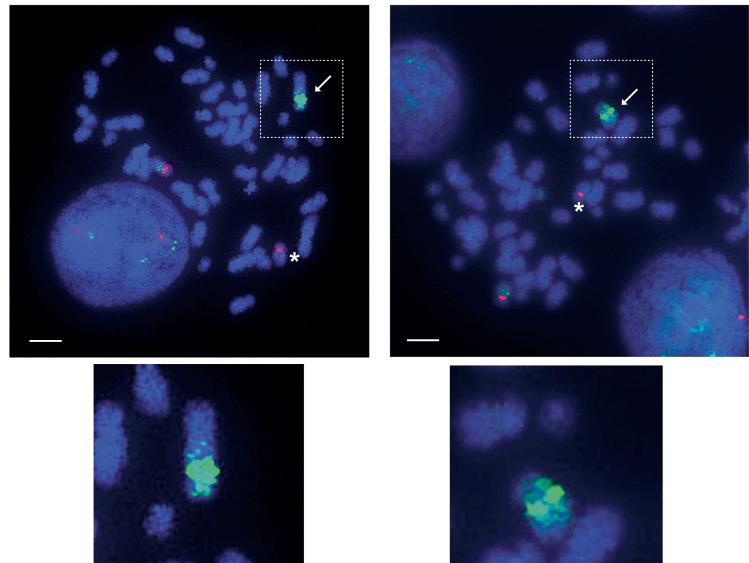
b



c



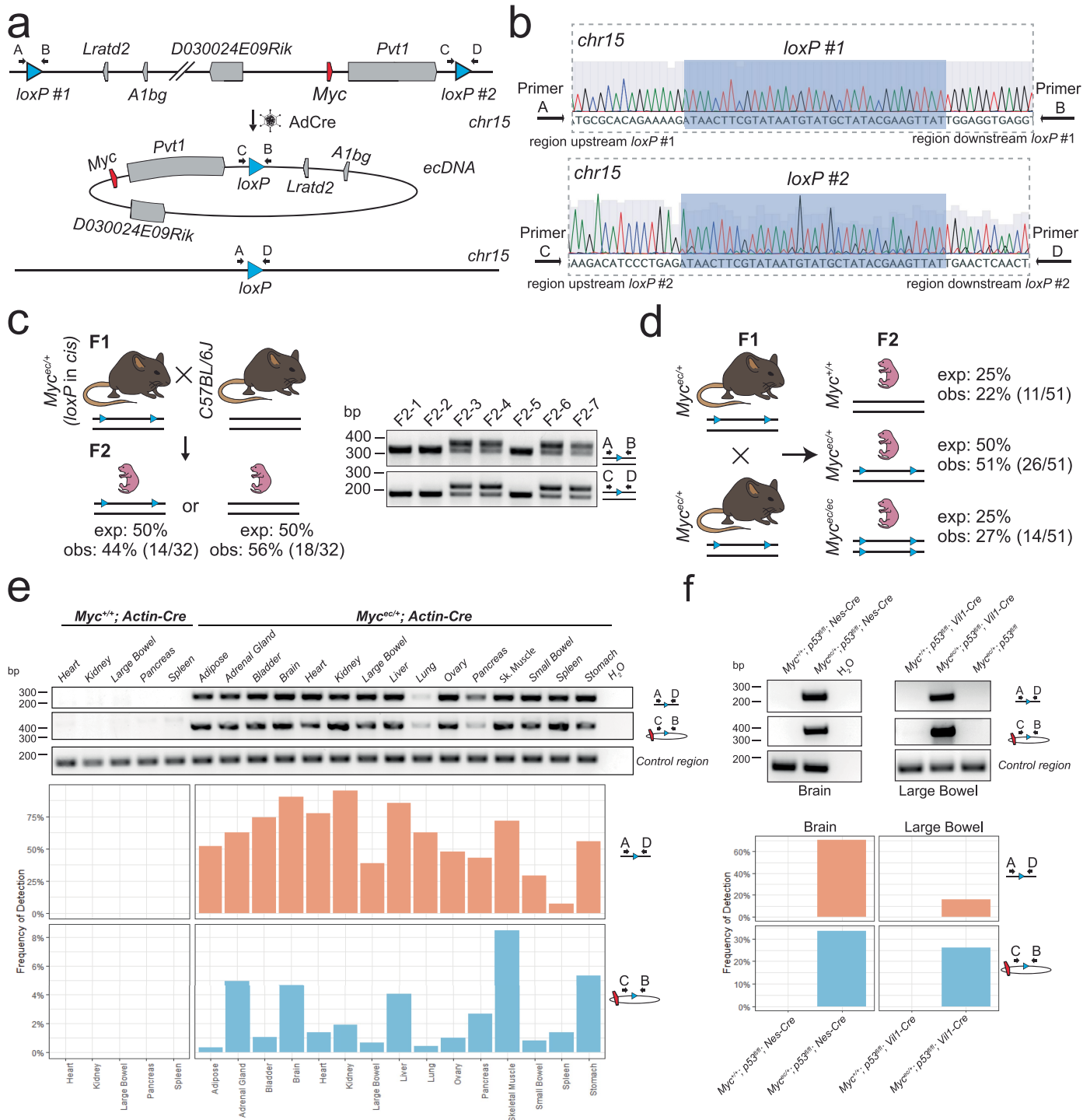
d



Extended Data Fig. 2 | Characterization of ecDNAs in ecMDM2 cells.

a. ecMDM2 and invMDM2 cells were infected with AdCre, expanded in the absence of hygromycin, and analyzed by flow cytometry at the indicated timepoints. Clones were propagated for 6 days in the presence or absence of hygromycin (200 µg/ml) and analyzed by flow cytometry. Pseudocolor scatter plots of GFP and mScarlet fluorescence at each time point are shown. Notice the progressive disappearance of double positive cells and the concomitant increase in GFP+;mScarlet+ cells in the ecMDM2 samples. b. Violin plots showing GFP intensity of sorted double positive ecMDM2 and invMDM2

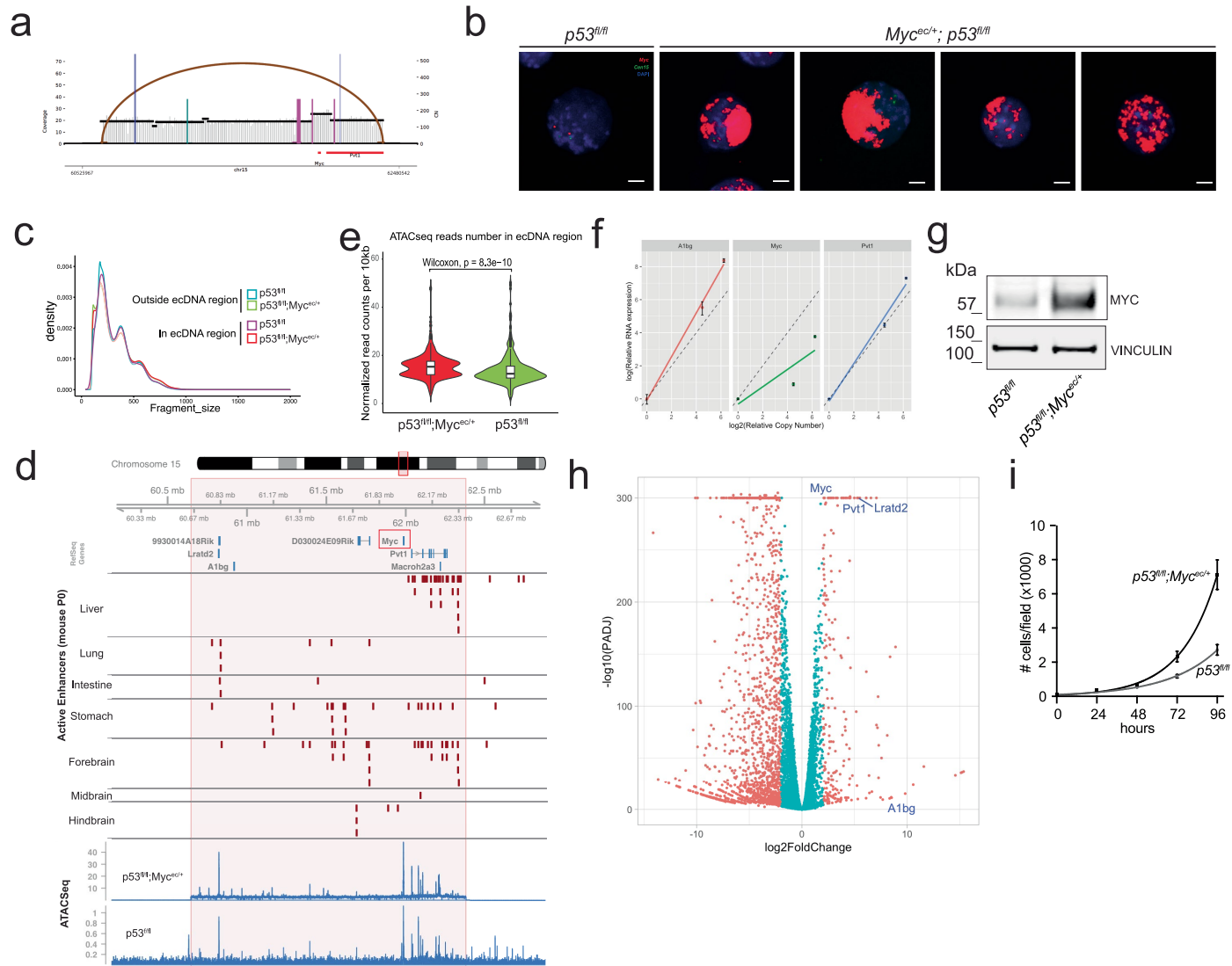
cells expanded in the presence of the indicated concentration of hygromycin for 13 days and analyzed by flow cytometry (see also Fig. 2F–H). Median GFP intensity for each sample is also indicated. Boxes indicated interquartile range. **** indicates p-value < 0.0001 as determined by the Wilcoxon–Mann–Whitney two-side test. c. Representative DNA FISH on metaphase spreads from ecMDM2 cells maintained at the indicated hygromycin concentration. Scale bar: 7.5 µm. n = 15 (No Hygro), 14 (0.2 mg/ml), 16 (1 mg/ml), 14 (5 mg/ml) metaphases analyzed. d. Presence of MDM2-positive HSRs in representative metaphase spreads (n = 6 HSR containing metaphases out of 91 analyzed). Scale bar: 7.5 µm.



Extended Data Fig. 3 | Generation and characterization of *Myc*^{ec/+} mice.

a. Schematic of the *Myc*^{ec} allele. Upon AdCre transduction, Cre recombinase promotes the excision and circularization of the genomic region flanked by the two *loxP* sites. Genes are indicated in gray boxes. *Myc* gene is highlighted in red. Arrows indicate primers to detect the insertion of *loxP*sites for genotyping and Sanger sequencing. **b.** Sanger sequencing results of inserted *loxP*sites in the F1 progeny. *LoxP* sequences in the correct orientation are highlighted in light blue. **c.** Breeding schemes to test viability and fertility of *Myc*^{ec/+} mice. Expected and observed genotypes in the F2 generation are reported. Representative genotyping PCR results are shown. All animals were genotyped. gDNA-PCR analysis to check for the insertion of both *loxP*sites (A-B and C-D) is shown on the left. **d.** Breeding schemes to test viability and fertility of *Myc*^{ec} mice. Expected and observed genotypes in the F2 generation are reported.

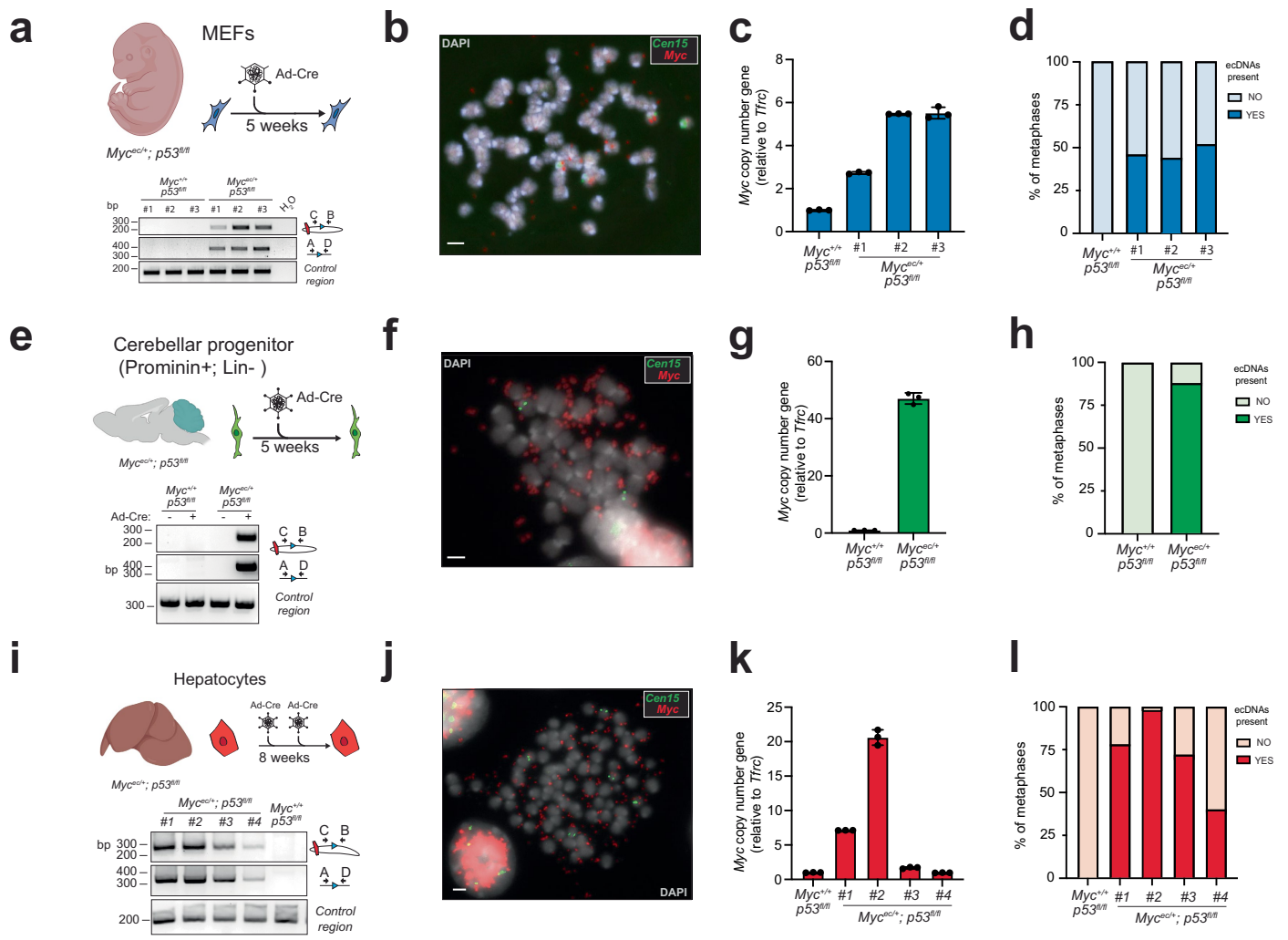
e. gDNA-PCR analysis with primers designed to detect the circularized allele (Primers C-B) and scar on the linear chromosome (Primers A-D) on the linear chromosome upon Cre-expression performed on DNA extracted from different tissues of a *Myc*^{ec/+}; *Actin-Cre* mouse (1 month old). Amplification of an unrelated genomic region is included as a PCR control. Quantification by digital droplet PCR (ddPCR) of the circularized allele (Probes c-b) and the scar in linear chromosome (Probes a-d) is shown at the bottom. Heart, kidney, large bowel, pancreas, and spleen of a single *Myc*^{ec/+}; *Actin-Cre* mouse are used as controls. **f.** gDNA-PCR analysis (top) and quantification by ddPCR (bottom) of the circularized allele and the scar in linear chromosome in brain and large intestine of mice expressing the Cre recombinase under the control of the tissue-specific promoter of Nestin and Villin1 (*Vil1*), respectively. The genotype of each mouse is indicated.



Extended Data Fig. 4 | Characterization of ecDNAs in Myc^{ec/+} NSCs.

a. sWGS data from the 5 week time points (see Fig. 3B) were analyzed using AmpliconArchitect to identify structural variants. The structural variant plot reveals a structural variant closing the left-and-right endpoints of the amplified region forming an ecDNA-like cycle spanning the region flanked by the *loxP* sites. **b.** Representative interphase-nuclei FISH (right) on aNSC from Myc^{ec/+}; p53^{fl/fl} 5 weeks upon AdCre infection showing clustering inside the nucleus. Myc probe is in red. Control probe labeling a pericentromeric region of chromosome 15 is in green. Scale bar: 5 μ m. **c.** ATAC-seq fragment size distribution of ecDNA and chromosomal DNA regions. n = 2 replicate per group. **d.** Location of active enhancers contained within and immediately outside the Myc ecDNA. Enhancers from the indicated mouse tissues at birth (PO) were obtained from the Encyclopedia of DNA elements (ENCODE) (ref. 59). The two bottom tracks show ATAC-Seq reads count across the same region generated from NSCs with the indicated genotypes. The region corresponding to the ecDNA is highlighted in light red. **e.** ATAC-seq read counts in Myc^{ec} region normalized by sequencing

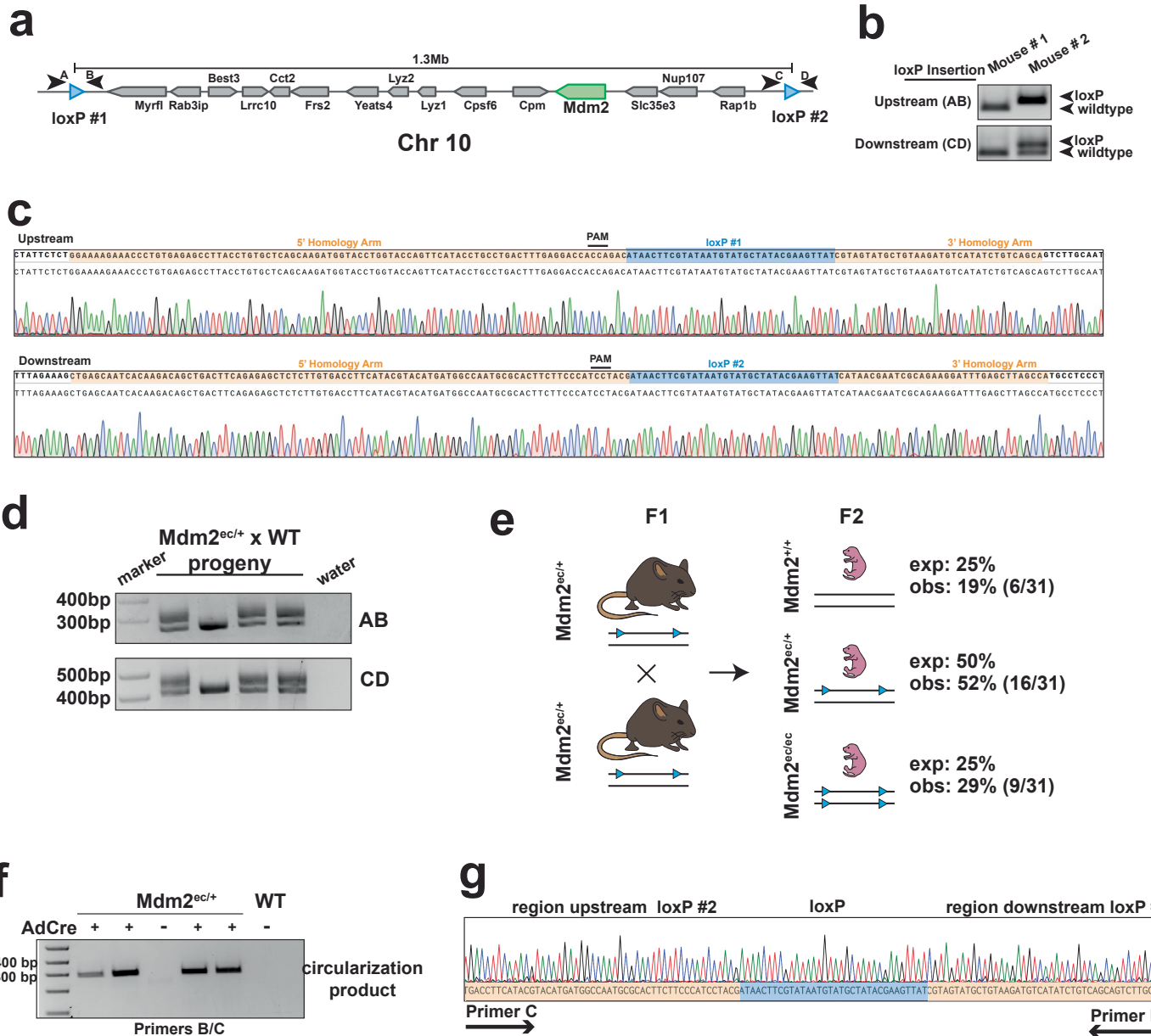
depth and copy number in p53^{fl/fl};Myc^{ec/+} and p53^{fl/fl} cells (5,001,487 and 58,957 reads, respectively). Boxes indicate upper quartile, median, and lower quartile. Whiskers extend to $\pm 1.5 \times$ IQR. Two-sided Wilcoxon test. P value = 8.3e-10. **f.** Relative copy number and mRNA expression were determined by qPCR in Myc^{ec/+};p53^{fl/fl} neuronal stem cells at 1 week, 3 weeks, and 5 weeks post Ad-Cre infection. Only genes within the amplicon detectable at baseline are shown. Note that A1bg and Pvt1 expression increases more than predicted based on copy number (dashed line), while Myc expression increase is lower than predicted. **g.** Immunoblotting of MYC expression levels in Myc^{ec/+}; p53^{fl/fl} and p53^{fl/fl} aNSC 5 weeks upon AdCre Infection. **h.** Volcano plot of Myc^{ec/+};p53^{fl/fl} vs p53^{fl/fl} aNSC 5 weeks upon AdCre infection. Genes with log₂ Fold Change > 1, and adjusted P-value calculated using the DESeq2R package < 0.01 are indicated in red. Genes located in the Myc^{ec} amplicon are labeled. **i.** Growth curves of Myc^{ec/+}; p53^{fl/fl} (black) and control p53^{fl/fl} (grey) aNSC 5 weeks after AdCre infection. n = 10 biological replicates, 3 fields for each replicate have been acquired.



Extended Data Fig. 5 | Generation of Myc-containing ecDNAs in different primary cell types. *Myc*^{ec/+}; *p53*^{fl/fl} and *Myc*^{+/+}; *p53*^{fl/fl} primary mouse embryo fibroblasts (**a-d**), cerebellar stem cells (**e-h**), and primary hepatocytes (**i-l**) were infected with Cre recombinase, passaged for 5–8 weeks and analyzed by PCR to detect circularization and excision of the ecDNA allele (**a, e, i**). (**b, f, j**) Metaphase spreads were examined by DNA-FISH using a Myc probe. Scale bar = 5 μm (**c, g, k**).

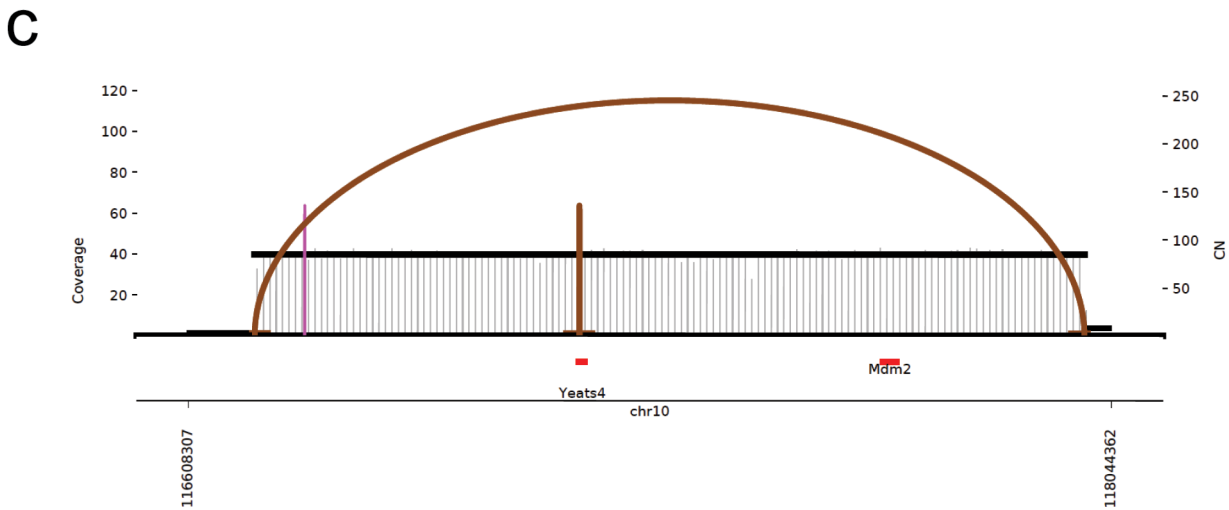
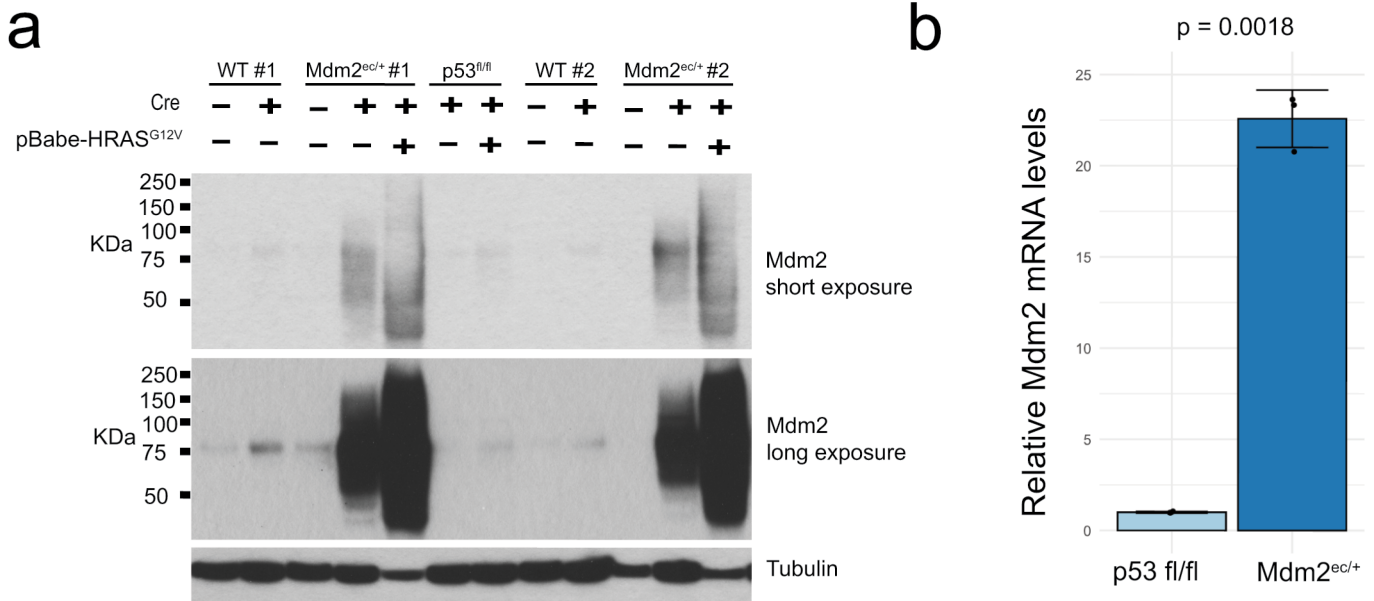
Total genomic DNA was used to determine mean Myc copy number. Each bar corresponds to a biological replicate. (Error bars: mean ± SD). (**d, h, l**) Stacked bar plot showing the fraction of metaphases with (dark color) or without (light color) detectable Myc positive double minutes (ecDNAs). n = 50 metaphases per bar. Illustrations in **a, b** and **i** were created using BioRender (<https://biorender.com>).

Article



Extended Data Fig. 6 | Generation and characterization of Mdm2^{ec/+} mice.
a. Schematic of the Mdm2ec allele, with the two loxP sites flanking a 1.3Mb region on chromosome 12. Arrowheads indicate the PCR primers used to identify successful loxP insertion. **b.** Zygotes were injected with Cas9-gRNA complexes and donor DNA containing loxP sites. Genotyping of F0 mice shows that Mouse #2 has loxP sites inserted at both the upstream and downstream locations. Note that the upstream wildtype band for Mouse #2 is lost, in this case indicating homozygous insertion of the loxP. After initial validation by sequencing, all mice were genotyped by PCR. **c.** Chromatograms showing correct insertion of the two loxP sites. **d.** A heterozygote F1 progeny of Mouse

#2 crossed to a wildtype mouse shows that the loxP bands for the upstream and downstream integration sites co-segregate in the resulting F2 progeny, indicating that the loxP sites were inserted in cis. **e.** Mdm2^{ec/+} F1 mice are bred to each other and resulting expected and observed F2 progeny ratio are described. **f.** AdCre-treated Mdm2^{ec/+} MEFs develop recombination of the loxP sites, resulting in the circularization of the intervening region as indicated by the amplification product of primers B and C. Repeated in three independent experiments. **g.** Chromatogram obtained by Sanger sequencing of the circularization product from E) demonstrated expected recombination sequence surrounding the loxP site.

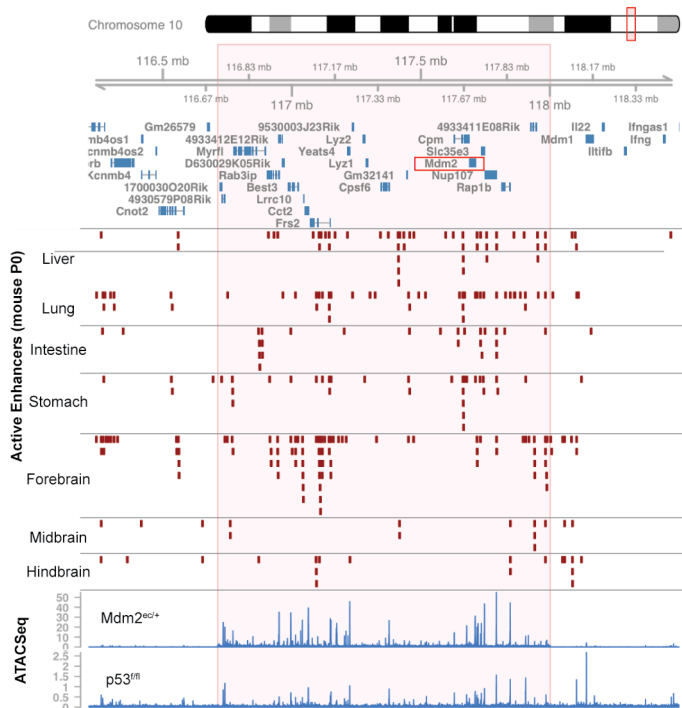


Extended Data Fig. 7 | Mdm2 expression in Mdm2^{ec/+} MEFs. **a.** Western blot for MDM2 and tubulin of wildtype, *Mdm2*^{ec/+}, and *p53*^{fl/fl} MEFs with or without treatment by Cre and HRAS^{G12V} show significant accumulation of Mdm2 only in Cre-treated *Mdm2*^{ec/+} MEFs. Biological replicates from different *Mdm2*^{ec/+} MEF lines were analyzed. **b.** qPCR in Cre-treated *Mdm2*^{ec/+}, and *p53*^{fl/fl} MEFs show preferential upregulation of Mdm2 transcripts in *Mdm2*^{ec/+} MEFs. p -value: 0.0018,

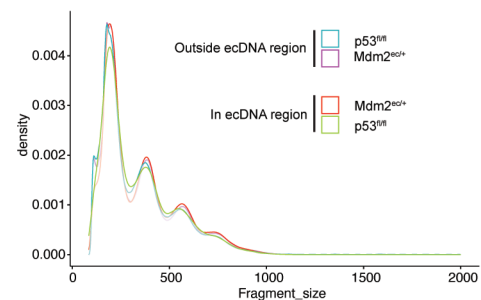
two-tailed t-test, Error bars: mean \pm SD. N = 3 technical replicates. **c.** sWGS data from AdCre- and HRAS infected *Mdm2*^{ec/+} MEFs (see Fig. 4) were analyzed using AmpliconArchitect to identify structural variants. The coverage and structural variant plot reveals a structural variant closing the left-and-right endpoints of the amplified region forming an ecdNA-like cycle spanning the region flanked by the *loxP*sites.

Article

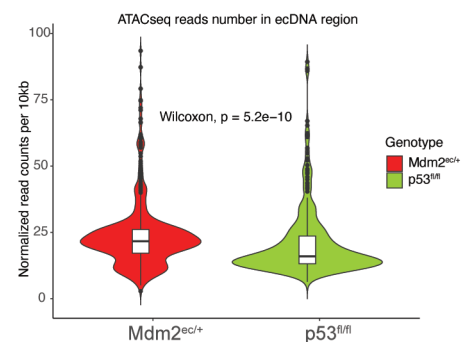
a



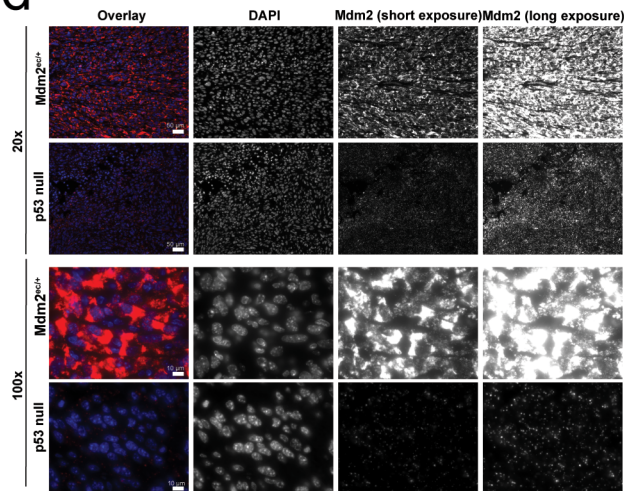
b



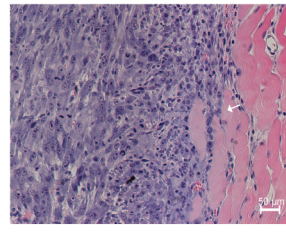
c



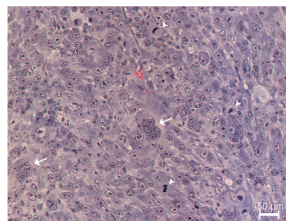
d



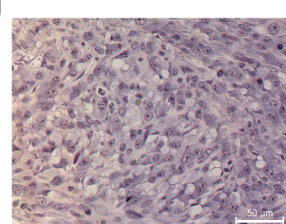
e



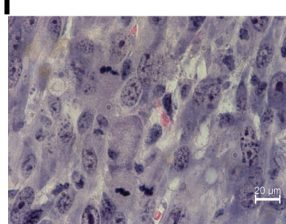
f



g



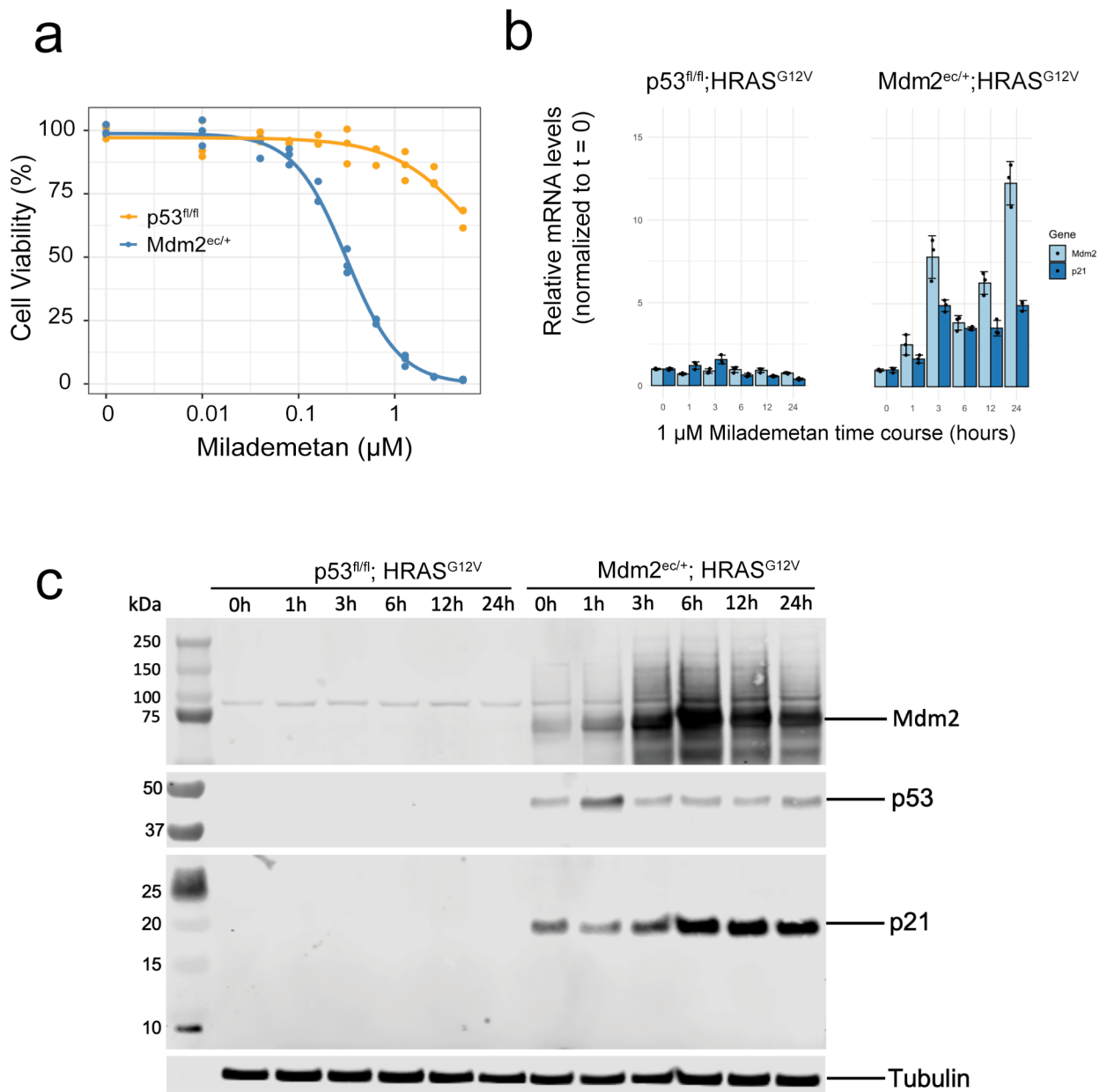
h



Extended Data Fig. 8 | Characterization of *Mdm2*^{ec/+};HRAS^{G12V} sarcomas.

a. Location of active enhancers contained within and immediately outside the *Mdm2* ecDNA. Enhancers from the indicated mouse tissues at birth (P0) were obtained from the Encyclopedia of DNA elements (ENCODE) (ref. 59). The two bottom tracks show ATAC-Seq reads count across the same region generated from NSCs with the indicated genotypes. The region corresponding to the ecDNA is highlighted in light red. **b.** ATAC-seq fragment size distribution of ecDNA and chromosomal DNA regions in *Mdm2*^{ec/+} and *p53*^{f/f} MEFs transduce with HRAS^{G12V}. $n=4$ replicates for *Mdm2*^{ec/+} and 3 replicates for *p53*^{f/f}. **c.** ATAC-seq read counts in *Mdm2*^{ec} region normalized by sequencing depth and copy number in *Mdm2*^{ec/+}, *p53*^{f/f} and *p53*^{ff} cells. (3,693,906 and 108,897 reads, respectively). Boxes indicate upper quartile, median, and lower quartile. Whiskers extend to $\pm 1.5 \times$ IQR. Two-sided Wilcoxon test. P value = 5.2e-10.

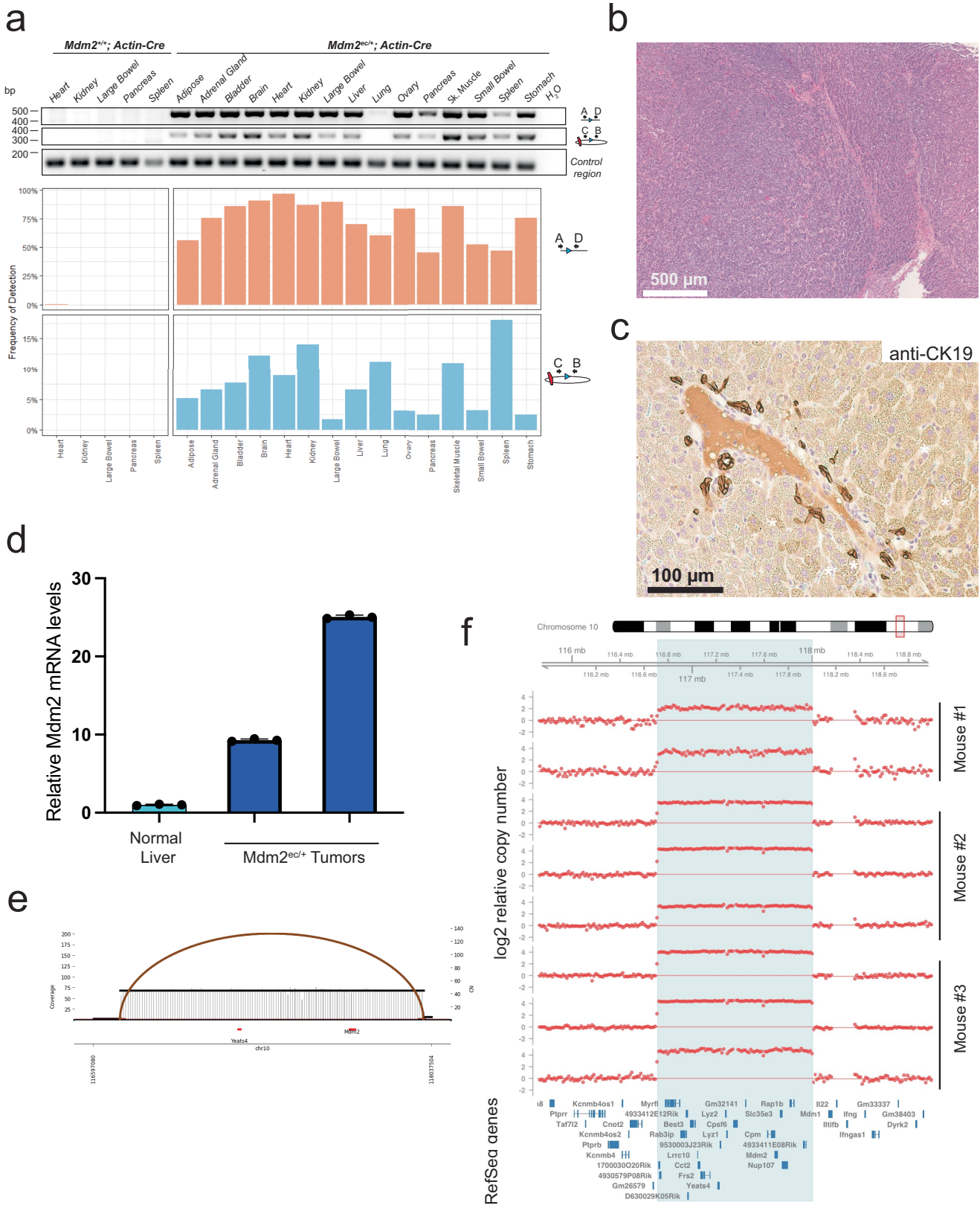
d. RNA-FISH using an *Mdm2* probe on tumour tissues from *Mdm2*^{ec/+};HRAS^{G12V} and *p53*^{ff};HRAS^{G12V} MEFs at both low (20x, scale bar = 50 µm) and high (100x, scale bar = 10 µm) magnifications. **e.** Low magnification view showing a high-grade spindle cell sarcoma arranged in short fascicles and infiltrating into skeletal muscle. **f.** The lesional cells show increased nuclear pleomorphism, with scattered multinucleated forms (arrows) and increased mitotic activity (arrowheads). **g.** Higher magnification shows solid sheets of epithelioid to ovoid cells with distinct single or multi-intra-cytoplasmic fat vacuoles consistent with signet ring lipoblasts. Focal nuclear indentation, a characteristic feature of lipoblasts, is also noted. **h.** Increased mitotic activity and pleomorphic spindle cells with amphophilic cytoplasm and ovoid nuclei with clumped chromatin and prominent nucleoli in keeping with a high-grade sarcoma. Analysis repeated in tumours from 3 mice.



Extended Data Fig. 9 | Mdm2^{ec/+};HRAS^{G12V} sarcomas response to Milademetan. **a.** Dose-response curve of AdCre-treated *p53^{fl/fl};HRAS^{G12V}* and *Mdm2^{ec/+};HRAS^{G12V}* cells treated with the MDM2 antagonist milademetan. Each dot represents a technical replicate ($n = 3$). A representative plot of two independent experiments is shown. **b-c.** Cre-treated *Mdm2^{ec/+};HRAS^{G12V}* and

p53^{fl/fl};HRAS^{G12V} MEFs were exposed to 1 μ M milademetan, collected at indicated time points, and analyzed by RT-qPCR (b) and immunoblot (c). Error bars: mean \pm SD. N = 3 technical replicates. Mdm2 and p21 mRNA and protein products are rapidly induced in *Mdm2^{ec/+};HRAS^{G12V}* cells in response to milademetan.

Article



Extended Data Fig. 10 | See next page for caption.

Extended Data Fig. 10 | Characterization of *Mdm2*^{ec/+};Myc^{tg} liver tumours.

a. gDNA-PCR analysis with primers designed to detect the circularized allele (Primers C-B) and allele excision (Primers A-D) on the linear chromosome upon Cre-expression performed on DNA extracted from different tissues of *Mdm2*^{ec/+};*Actin-Cre* mouse (1 month old). Amplification of an unrelated genomic region is included as a PCR control. Quantification by digital droplet PCR (ddPCR) of the circularized allele (Probes C-B) and excision from the linear chromosome (Probes A-D) is shown at the bottom. Heart, kidney, large bowel, pancreas, and spleen of *Mdm2*^{+/+};*Actin-Cre* mouse are used as controls. **b.** Lower magnification of a representative H&E of *Mdm2*^{ec/+} liver tumour, showing the primary tumour is a poorly differentiated hepatocellular carcinoma (scale bar = 500 μ m).

c. Representative CK19 staining with a CK19+ bile duct, indicating tumours are negative for the cholangiocyte marker CK19 (scale bar = 100 μ m, n = tumours from 3 mice). **d.** qPCR analysis of *Mdm2* mRNA expression levels in *Mdm2*^{ec/+} tumours compared to normal liver. Error bars; mean \pm SD. N = 3 technical replicates. **e.** sWGS data from a representative *Mdm2*^{ec/+} tumour were analyzed using Amplicon Architect to identify structural variants. The structural variant plot reveals a structural variant closing the left-and-right endpoints of the amplified region forming an ecDNA-like circle spanning the region flanked by the *loxP* sites. All tumours analyzed from three mice showed the same circular amplicon. **f.** sWGS analysis of individual liver tumours from three *Actin-Cre*; *Mdm2*^{ec/+} mice.

Reporting Summary

Nature Portfolio wishes to improve the reproducibility of the work that we publish. This form provides structure for consistency and transparency in reporting. For further information on Nature Portfolio policies, see our [Editorial Policies](#) and the [Editorial Policy Checklist](#).

Statistics

For all statistical analyses, confirm that the following items are present in the figure legend, table legend, main text, or Methods section.

n/a Confirmed

- The exact sample size (n) for each experimental group/condition, given as a discrete number and unit of measurement
- A statement on whether measurements were taken from distinct samples or whether the same sample was measured repeatedly
- The statistical test(s) used AND whether they are one- or two-sided
Only common tests should be described solely by name; describe more complex techniques in the Methods section.
- A description of all covariates tested
- A description of any assumptions or corrections, such as tests of normality and adjustment for multiple comparisons
- A full description of the statistical parameters including central tendency (e.g. means) or other basic estimates (e.g. regression coefficient) AND variation (e.g. standard deviation) or associated estimates of uncertainty (e.g. confidence intervals)
- For null hypothesis testing, the test statistic (e.g. F , t , r) with confidence intervals, effect sizes, degrees of freedom and P value noted
Give P values as exact values whenever suitable.
- For Bayesian analysis, information on the choice of priors and Markov chain Monte Carlo settings
- For hierarchical and complex designs, identification of the appropriate level for tests and full reporting of outcomes
- Estimates of effect sizes (e.g. Cohen's d , Pearson's r), indicating how they were calculated

Our web collection on [statistics for biologists](#) contains articles on many of the points above.

Software and code

Policy information about [availability of computer code](#)

Data collection

- Flow cytometry: LSR Fortessa (BD biosciences);
- FACS: FACSAria (BD biosciences) and FACSymphony (BD biosciences);
- qPCR and CNV assays: QuantStudio™ 6 Flex real-time PCR system;
- Metaphase spreads and FISH: AX10 Imager.Z1 Zeiss microscope, Zeiss Axioplan 2i epifluorescence microscope (Carl Zeiss Microscopy, Thornwood, NY);
- Dose-response curve: Synergy 2 plate reader (Bioteck);
- WB: Odyssey Imaging System (LICOR);

Data analysis

- Shallow Whole-Genome Sequencing (sWGS): Bowtie2 aligner, the QDNAseq R package, Gviz package;
- Image analysis: Fiji (version 2.0.0-rc-65/1.15w) and Isis imaging software (MetaSystem);
- RNASEq: STAR aligner and DESeq2 R package
- ddPCR: QuantaSoft software (Bio-Rad; Version 1.7)
- Amplicon Architect: AmpliconSuite-pipeline (version 0.1555.1), AmpliconArchitect (version 0.9.9).
- For statistical analysis: GraphPad Prism 9 and R

For manuscripts utilizing custom algorithms or software that are central to the research but not yet described in published literature, software must be made available to editors and reviewers. We strongly encourage code deposition in a community repository (e.g. GitHub). See the Nature Portfolio [guidelines for submitting code & software](#) for further information.

Data

Policy information about [availability of data](#)

All manuscripts must include a [data availability statement](#). This statement should provide the following information, where applicable:

- Accession codes, unique identifiers, or web links for publicly available datasets
- A description of any restrictions on data availability
- For clinical datasets or third party data, please ensure that the statement adheres to our [policy](#)

All datasets have been deposited and made publicly available: shallow Whole Genome sequencing data (GSE264005), bulk RNAseq data (GSE264003), and ATACseq data (GSE264240). AmpliconArchitect outputs for murine Mdm2-containing ecDNA (<https://ampliconrepository.org/project/649b3c097dc54138a9d391b3>) and murine Myc-containing ecDNA (<https://ampliconrepository.org/project/64839f137dc54138a9d39122>) are available through the AmpliconRepository online repository (<https://ampliconrepository.org/>).

Materials are available from the corresponding authors upon reasonable request. Plasmids containing the “circularization cassettes” described in this paper are available through Addgene. Mycec (Strain: #039221) and Mdm2ec (Strain: #039222) strains will be available through the JAX repository.

Research involving human participants, their data, or biological material

Policy information about studies with [human participants or human data](#). See also policy information about [sex, gender \(identity/presentation\), and sexual orientation](#) and [race, ethnicity and racism](#).

Reporting on sex and gender

n/a

Reporting on race, ethnicity, or other socially relevant groupings

n/a

Population characteristics

n/a

Recruitment

n/a

Ethics oversight

n/a

Note that full information on the approval of the study protocol must also be provided in the manuscript.

Field-specific reporting

Please select the one below that is the best fit for your research. If you are not sure, read the appropriate sections before making your selection.

Life sciences

Behavioural & social sciences

Ecological, evolutionary & environmental sciences

For a reference copy of the document with all sections, see nature.com/documents/nr-reporting-summary-flat.pdf

Life sciences study design

All studies must disclose on these points even when the disclosure is negative.

Sample size

For in vivo experiments, we evaluated the sample size by G.Power software considering a multifactorial variance analysis. The rationale for this was to reduce to a minimum the number of animals used, according to the 3R principle for animal care. For all other experiments, no statistical methods were used to predetermine sample size. Sample sizes were estimated on the basis of previous experiments conducted in our laboratory providing a sufficient numerosity for each group to yield a two-sided statistical test that can reach a power of 0.9 (subject to alpha= 0.05).

Data exclusions

No data were excluded for pre-established criteria.

Replication

To verify their reproducibility, experiments were successfully repeated using different batches of reagents, and different stocks of cell lines and, for some experiments, were repeated and confirmed by different operators.

Randomization

For in vitro experiments, samples were randomly treated according to the experimental design. For in vivo experiments, mice were injected independently of their genotype.

Blinding

When possible, data analysis were performed blind (including quantification of ecDNA per metaphases).

Reporting for specific materials, systems and methods

We require information from authors about some types of materials, experimental systems and methods used in many studies. Here, indicate whether each material, system or method listed is relevant to your study. If you are not sure if a list item applies to your research, read the appropriate section before selecting a response.

Materials & experimental systems

n/a	Involved in the study
<input type="checkbox"/>	<input checked="" type="checkbox"/> Antibodies
<input type="checkbox"/>	<input checked="" type="checkbox"/> Eukaryotic cell lines
<input checked="" type="checkbox"/>	<input type="checkbox"/> Palaeontology and archaeology
<input type="checkbox"/>	<input checked="" type="checkbox"/> Animals and other organisms
<input checked="" type="checkbox"/>	<input type="checkbox"/> Clinical data
<input checked="" type="checkbox"/>	<input type="checkbox"/> Dual use research of concern
<input checked="" type="checkbox"/>	<input type="checkbox"/> Plants

Methods

n/a	Involved in the study
<input checked="" type="checkbox"/>	<input type="checkbox"/> ChIP-seq
<input type="checkbox"/>	<input checked="" type="checkbox"/> Flow cytometry
<input checked="" type="checkbox"/>	<input type="checkbox"/> MRI-based neuroimaging

Antibodies

Antibodies used

anti-VINCULIN (1:5,000; Millipore, #MAB3574), anti-c-MYC (1:1,000; Cell Signaling, #D84C12), anti-MDM2 (1:1000, Cell Signaling, #51541), anti-alpha-tubulin (1:5000, Cell Signaling, #3873), anti-p53 (1:1000, Leica Biosystems, P53-PROTEIN-CMS), anti-p21 (1:1000, Cell Signaling, #64016), anti-HNF4a (Cell Signaling #3113T; 1:500), anti-CK19 (Abcam #AB52625, 1:500).
The following secondary antibodies were used: IRDye 800 anti-Rabbit (#926-32213, LICOR) and IRDye 680 anti-Mouse (#926-68072, LICOR). VectaStain ABC-HRP Rabbit IgG (Vector Laboratories #PK-6101). The following secondary antibodies were used to isolate cerebellar stem cells: Cd133 (Prominin-1), Monoclonal Antibody (13A4)-FITC (311-1331-80; Thermo Scientific. 1:100); Cd81 Monoclonal Antibody (Eat2)-PE (#MA517941; Thermo Scientific. 1:50); Anti-O4-PE (#130-117-507; Miltenyi Biotec. 1:50); Anti-PSA-NCAM-PE (#130-117-394; Miltenyi Biotec. 1:50).

Validation

All antibodies are commercially available and were tested for species and application as described in each manufacturer's protocol:

 anti-VINCULIN: 100% Performance Guaranteed validated antibodies
 anti-c-MYC: validated by Cell Signaling in c-Myc knockout HEK293 cells
 anti-MDM2 (Cell Signaling): Tested by Cell Signaling in SJS-A-1, Saos-2 (human), C2C12 (mouse), and MTLn3 (rat) cells, untreated (-) or treated with Nutlin 3a. Independently validated in our lab using Mdm2 KO MEFs.
 anti-alpha-tubulin: Tested by Cell Signaling in Hela and COS-7
 anti-p53: validated upon Doxorubicin treatment of MEF
 anti-p21: Tested by Cell Signaling in control or Nutlin-3a-treated C2C12 cells.
 anti-HNF4a: validated by Cell Signaling in HepG2 cells expressing an antigen specific peptide or a control peptide.
 anti-CK19: validate in 35 publications for the same species (mouse) and application (IHC)
 anti-Cd133-FITC: Tested by ThermoFisher in flow cytometric analysis of mouse bone marrow cells
 anti-Cd81-PE: Tested by ThermoFisher in flow cytometric analysis of mouse splenic B cells.
 anti-O4-PE: Tested on mouse brain tissue postnatal day 6 dissociated using the Neural Tissue Dissociation Kit (P) and the gentleMACS™ Dissociator.
 anti-PSA-NCAM-PE: Tested on mouse brain tissue postnatal day 1 dissociated using the Neural Tissue Dissociation Kit (T).

Eukaryotic cell lines

Policy information about [cell lines and Sex and Gender in Research](#)

Cell line source(s)

HCT116 cells (ATCC, CCL-247).
MEF, aNSC, cerebellar stem cells, and primary hepatocytes were derived from our generated GEMM.

Authentication

HCT116 were directly purchase from ATCC and targeted at passage 2. ATCC provided the following authentication based on STR profiling (Amelogenin: X,Y; CSF1PO: 7,10; D13S317: 10,12; D16S539: 11,13; D5S818: 10,11; D7S820: 11,12; TH01: 8,9; TPOX: 8,9; vWA: 17,22) (ATCC Cell Line Authentication Service - Sanger Sequencing).

Mycoplasma contamination

All cells were tested for mycoplasma contamination.

Commonly misidentified lines (See [ICLAC](#) register)

n/a

Animals and other research organisms

Policy information about [studies involving animals; ARRIVE guidelines](#) recommended for reporting animal research, and [Sex and Gender in Research](#)

Laboratory animals

Mouse

Wild animals

n/a

Reporting on sex

Findings apply to both sexes. HCT116 cells have been derived from the colon of an adult male with colon cancer. In mouse primary cells, ecDNA formation was demonstrated in both male and females-derived cell lines.

Field-collected samples

n/a

Ethics oversight

All animal experiments were approved by MSKCC's Institutional Animal Care and Use Committee.

Note that full information on the approval of the study protocol must also be provided in the manuscript.

Flow Cytometry

Plots

Confirm that:

- The axis labels state the marker and fluorochrome used (e.g. CD4-FITC).
- The axis scales are clearly visible. Include numbers along axes only for bottom left plot of group (a 'group' is an analysis of identical markers).
- All plots are contour plots with outliers or pseudocolor plots.
- A numerical value for number of cells or percentage (with statistics) is provided.

Methodology

Sample preparation

Single cell suspension were obtained by trypsin-mediated dissociation of adherent cells. Before sorting or flow cytometry analysis cells were filtered through a 70 µm strainer to remove cell aggregates.

Instrument

LSR Fortessa (BD biosciences), FACSaria (BD biosciences), and FACSymphony (BD biosciences).

Software

BDFACSDiva software was used to collect data and FlowJo (v10.8) was used for analysis.

Cell population abundance

The entire population was analyzed. Post-sorting fractions were re-analyzed to confirm the purity of each fraction.

Gating strategy

Cells were first gated based on the size (FSC) and the density/granularity (SSC), excluding debris and doublets; DAPI staining was used to gate the live fraction. Then, polygonal or quadrant gates were applied to isolate the population of interest based on GFP, mScarlet, FITC, or PE expression. The gating strategy of the relevant figures is provided in the file supplementary information file containing the uncropped gel images.

- Tick this box to confirm that a figure exemplifying the gating strategy is provided in the Supplementary Information.